ELSEVIER SAUNDERS

POSITRON EMISSION TOMOGRAPHY

PET Clin 2 (2007) 191–217

Advances in Attenuation Correction Techniques in PET

Habib Zaidi, PhD, PD[a,*], Marie-Louise Montandon, PhD[a], Abass Alavi, MD[b]

In positron emission tomography (PET), the imaging system records two antiparallel 511 keV photons that are emitted after electron–positron annihilation. In this case, the annihilation photons traverse a total tissue thickness that is equal to the body thickness intersected by the line between the two detectors, also called the line of response (LoR). Since its inception, photon attenuation in biological tissues has been identified as the most important physical degrading factor affecting PET image quality and quantitative accuracy [1]. Photon attenuation usually refers to the combination of photoelectric absorption and Compton scattering. That is, both are components of the general process of photon attenuation [2].

A particularity of PET (in contrast to single-photon emission computed tomography - SPECT) is that the attenuation factor for a given LoR depends on the total distance traveled by both annihilation photons within the attenuating medium, and it is independent of the emission (EM) point along this LoR. This makes attenuation correction (AC) easier, owing to the fact that it only requires a simple premultiplication of the EM data by the resultant

This work was supported by Grant Number SNSF 3100A0-116547 from the Swiss National Foundation.
[a] Division of Nuclear Medicine, Geneva University Hospital, CH-1211 Geneva 4, Switzerland
[b] Division of Nuclear Medicine, Department of Radiology, Hospital of the University of Pennsylvania, 3400 Spruce Street, Philadelphia, PA 19104, USA
* Corresponding author.
E-mail address: habib.zaidi@hcuge.ch (H. Zaidi).

1556-8598/07/$ – see front matter
doi:10.1016/j.cpet.2007.12.002
pet.theclinics.com

attenuation correction factors (ACFs). Yet, the ACFs in PET are huge, and quantitation is virtually impossible without compensating for the nonlinear attenuation effect. The magnitude of the ACFs required in PET often might exceed 100 for some LoRs through the body [3]. Various strategies have been devised to determine an accurate attenuation map to enable correction for photon attenuation in whole-body PET studies. Accurate attenuation compensation relies on robust determination of the attenuation map, which usually is derived through an external transmission (TX) scanning apparatus (eg, x-ray CT) integrated into the PET system design. The introduction of combined PET/CT scanners in the clinic has facilitated the AC process and allowed TX scanning time to decrease substantially compared with radionuclide TX scanning.

Thorough reviews of attenuation map derivation and AC techniques were published previously for nuclear medicine imaging in general [1,3], particularly for PET/CT [4], and more recently for cerebral PET imaging [5]. This article addresses this issue from a different perspective in the sense that it focuses on most recent developments in the field in general and the most promising approaches in particular. Given the widespread interest both in dual-modality PET/CT imaging and preclinical instrumentation, the pitfalls associated with CT-based attenuation correction and potential solutions and the unique problems of attenuation correction in small animal PET also are addressed. The physical and methodological bases of photon attenuation are addressed briefly, and state-of-the-art developments in algorithms used to derive the attenuation map aiming at accurate AC of PET data are summarized. Future prospects, research trends, and challenges are identified, and directions for future research are discussed.

What is photon attenuation?

The physical basis of photon attenuation lies in the natural property that annihilation photons emitted by the positron-emitting radiotracers (following positron–electron interaction) interact with human tissue and other materials as they travel through the body. The emitted annihilation photons have an energy of 511 keV and thus can undergo photoelectric interactions where the incident photon is absorbed completely, or more likely, can be scattered following interaction with loosely bound electrons in biological tissues. Scattering results in a change in the original direction of the incoming photon with (in the case of incoherent or Compton scattering) or without (in the case of coherent or Rayleigh scattering) energy loss. It should be emphasized that for soft tissue (the major constituent of the body), a moderately low atomic number (Z) material, two distinct regions of single interaction dominance can be differentiated: photoelectric below and Compton above 20 keV. In addition, the percentage of scattered events that undergo Compton interactions in the object is over 99.5% at 511 keV for soft tissues, which renders the number of interactions by photoelectric absorption or coherent scattering negligible.

In mathematical terms, the magnitude of photon attenuation can be expressed by the exponential equation:

$$I = I_o \exp\left[-\int_S \mu(s)\, ds\right] \quad (1)$$

where I_o and I are the incident and transmitted photon fluences, respectively, (in units of photons per unit area), and ds is a differential of the thickness of tissue encountered as the photon beam passes through the body along path S. The linear attenuation coefficient (μ) represents the probability that the photon will undergo an interaction while passing through a unit thickness of biological tissue. In other terms, the linear attenuation coefficient is a measure of the fraction of primary photons that interact while traversing an absorber, and the linear attenuation coefficient is expressed in units of inverse centimeters (cm^{-1}).

Fig. 1 illustrates typical reconstruction artifacts (depression of activity concentration in the center) resulting from the lack of AC for a uniform distribution of activity in a cylindric phantom. The figure shows a PET image reconstructed without AC, the CT-based attenuation map, the same slice obtained after applying AC but without scatter correction, and the same slice after applying attenuation and scatter corrections. Corresponding horizontal profiles drawn through the center of the slices also are shown (bottom row). Note the overestimation of activity distribution at the center of the cylinder before scatter correction and the recovery of a uniform activity distribution after attenuation and scatter compensations.

Practical and clinical consequences of photon attenuation

It is well established that PET images reconstructed without AC can introduce severe artifacts, hence obscuring subjective qualitative interpretation performed by nuclear medicine physicians and causing thoughtful inaccuracies when quantitative assessment of PET images is performed [6]. It is therefore imperative to be aware of the physical processes that underlie nonlinear photon attenuation, its clinical impact on reconstructed PET images, and

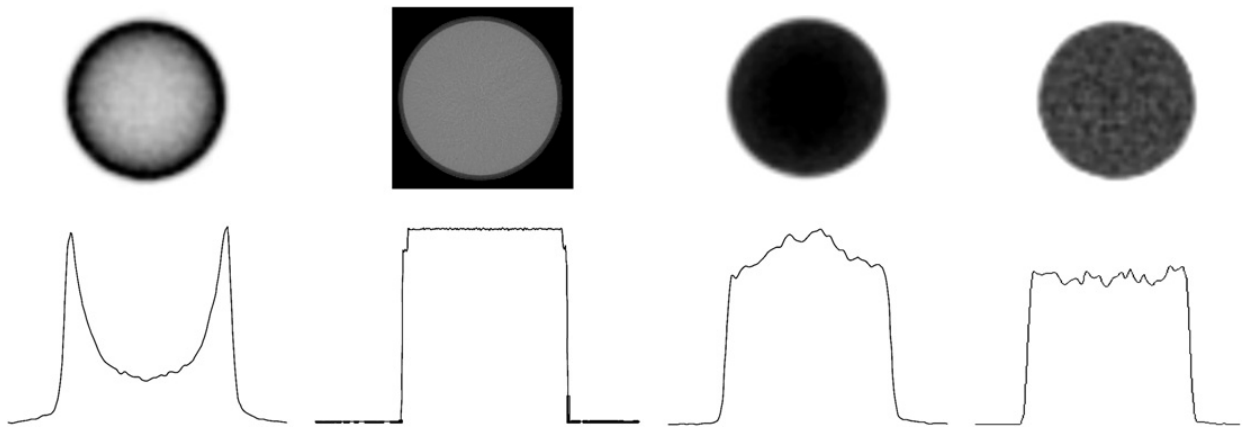

Fig. 1. Illustration of reconstruction artifacts resulting from the lack of attenuation correction for a uniform distribution of activity in a cylindric phantom (*top row*) and corresponding horizontal profiles drawn at the center of the cylinder (*bottom row*). From left to right: reconstructed image without attenuation correction, the CT-based attenuation map, the same slice after applying attenuation correction but without scatter correction, and finally the same slice after applying attenuation and scatter corrections. Note the loss of activity at the center of the cylinder on the noncorrected image, the overestimation of activity distribution at the center of the cylinder before scatter correction, and the recovery of a uniform activity distribution after attenuation and scatter corrections.

the performance of various methods that can be used to correct PET images for this physical degrading factor. AC in PET is widely accepted by the nuclear medicine community as a crucial part of data correction procedures that need to be applied for the production of artifact-free, quantitative PET data. It is should be noted that while the value of advanced techniques implemented on commercial clinical systems is no longer the subject of debate in cardiovascular imaging [7–10] and oncology imaging [11,12], there are still some controversies regarding their relevance in routine clinical brain studies where simple calculated techniques are available [5,13].

In realistic clinical situations, the magnitude of the error introduced by photon attenuation can vary regionally in reconstructed PET images, because the thickness of tissue varies for different regions of the patient's anatomy. Consequently, a lesion located deep within the body will produce a signal that is much highly attenuated compared with that for a superficial lesion. Likewise, a region containing a uniform activity distribution that lies beneath tissue having a variable thickness will produce an image with variable count density. This might happen in various situations such as myocardial perfusion/metabolism imaging where soft tissue attenuation caused by the diaphragm or breast tissue can produce false-positive defects [1]. Reconstruction of tomographic images without attenuation can cause erroneously high-count densities and reduced image contrast in low-attenuation regions such as the lung.

The literature reporting systematic comparative studies of the effect of different AC strategies in whole-body PET is impressive [1,4,5,14]. A limited number of studies, however, addressed the clinical impact of attenuation-corrected images versus no correction [15–24]. Nuyts and colleagues [25] modified the maximum-likelihood expectation maximization (ML-EM) reconstruction algorithm by allowing negative intensity values to compensate the loss of image detail in conventional ML-EM reconstructions, thus improving the visual quality of uncorrected whole-body PET images.

It is well accepted that AC increases statistical noise. In general, however, AC recovers the contrast lost and improves the quantitative accuracy and deep lesion detectability compared with the case where no correction is applied. The extent to which it can be shown mathematically that the lack of AC has a disabling effect upon the goal for which the image is to be used is a much more delicate issue to discuss and to corroborate. Fig. 2 shows a clinical whole-body PET study reconstructed without AC and images of the same study corrected for attenuation using measured TX scanning. The uncorrected image shows typical reconstruction artifacts (depression of activity concentration at the center) resulting from the lack of AC. More importantly, the mass (volume approximately 65cc; average standardized uptake value (SUV) approximately 2.1) apparent on the TX scan is clearly visible on the PET images reconstructed with AC but is not seen in the images without AC [12]. This is a clear argument supporting the need for AC in daily clinical PET examinations and against the claim that it has no impact on lesion detectability.

Methods for determination of the attenuation map

Various methods have been developed to compensate for photon attenuation in whole-body PET

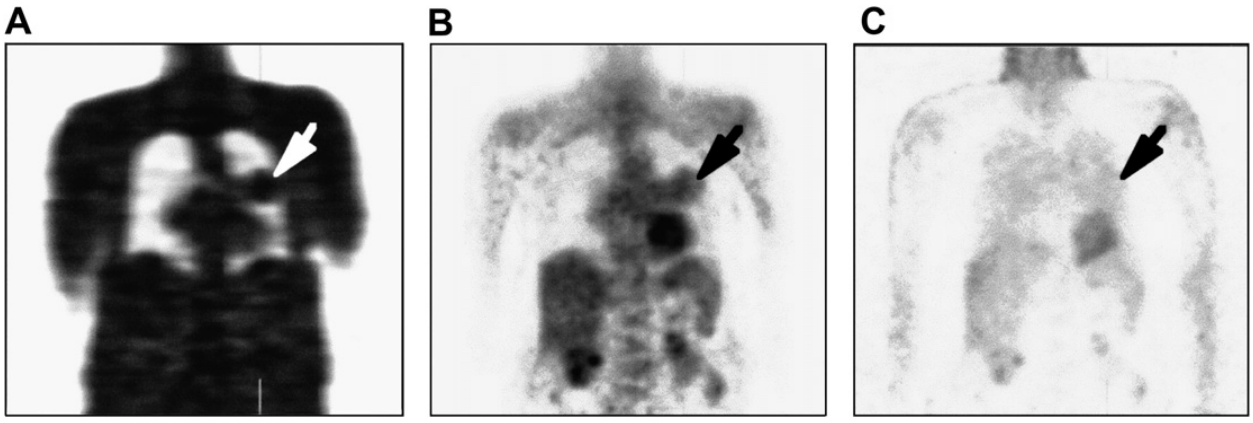

Fig. 2. Coronal sections of whole-body images of a patient with hamartoma (*arrow*), which is clearly visible as dense object in transmission image (*A*) and shows uptake of ^{18}F-FDG in attenuation-corrected emission image (*B*). In same image, plane of emission image reconstructed without attenuation correction (*C*); however, hamartoma is not detectable. (*Reprinted from* Bai C, Kinahan PE, Brasse D, et al. An analytic study of the effects of attenuation on tumor detection in whole-body PET oncology imaging. J Nucl Med 2003;44:1855–61; with permission.)

imaging. In a clinical setting, the balance between algorithmic complexity and the validity of results obtained is an important criterion when selecting an AC technique. Even though the methods that make a large number of assumptions frequently can be undemanding, it is not necessarily true that complex algorithms always will perform better. The extra complexity must be used judiciously and justified for the particular application at hand. In many cases, extra complexity can result just as easily in unreliability as in improved results. In a clinical setting, it has become standard practice to use simplified techniques compared with the often complex methods developed for research where there is greater emphasis on quantitative accuracy.

Methods that do not require a TX scan, often referred to as calculated methods, belong to the history of nuclear medicine, as they are considered to be obsolete with the introduction of dual-modality imaging systems. They still might be relevant (and likely will remain the method of choice) in brain PET imaging on research prototypes dedicated for brain research that are not equipped with TX scanning devices [26], or when radiation dose reduction (by elimination of the additional radiation dose contributed by the TX scan) is sought. These techniques are reviewed in Zaidi and colleagues [5].

In clinical and research settings, one needs to accommodate situations of nonuniform attenuation for which the spatial distribution of attenuation coefficients is not known a priori. Measured transmission-based AC is the most commonly used procedure in clinical and research settings, because it is expected to yield the best attenuation map as a result of matched energy and spatial resolution. Motion-induced misalignment between TX and EM scans, however, can result in erroneous estimation of regional tissue activity concentrations in cerebral [27,28], myocardial [29–34], and oncologic whole-body [35–42] imaging.

Fig. 3 shows a sketchy representation of different TX scanning sources and geometries and the expected quality of obtained attenuation maps. The TX sources include rotating positron-emitting (^{68}Ga/^{68}Ge) rods measuring TX in coincidence mode, single-photon point sources (^{137}Cs) producing coincidence events between the known source position and photons detected on the opposing side of the detector ring, and x-ray CT units combining a x-ray tube and detector on the opposite side typically used on modern combined PET/CT scanners. Note that x-ray CT produces the best possible diagnostic quality anatomic images, thus allowing an almost noise-free attenuation map to be derived. The high cost of dual-modality PET/CT units and the potential introduction of artifacts when using CT-based attenuation correction (CT-AC), which might disturb the visual interpretation of PET images and bias quantitative PET estimates, are major limitations of this approach, however. The previously mentioned techniques vary in complexity, accuracy, and computation time and will be described more in detail below.

Radionuclide-based transmission scanning

Before the advent of PET/CT, the most accurate means of determining a patient-specific attenuation map were based on measured radionuclide-based TX sources that could be acquired before (preinjection), during (simultaneous), or after (postinjection) the PET scan [3]. The first-generation PET scanners used TX ring sources of ^{68}Ga/^{68}Ge ($T_{1/2}$ = 68 minutes and 270.8 days, respectively), which coexist in secular equilibrium, whereas the second-generation scanners used on average one or more

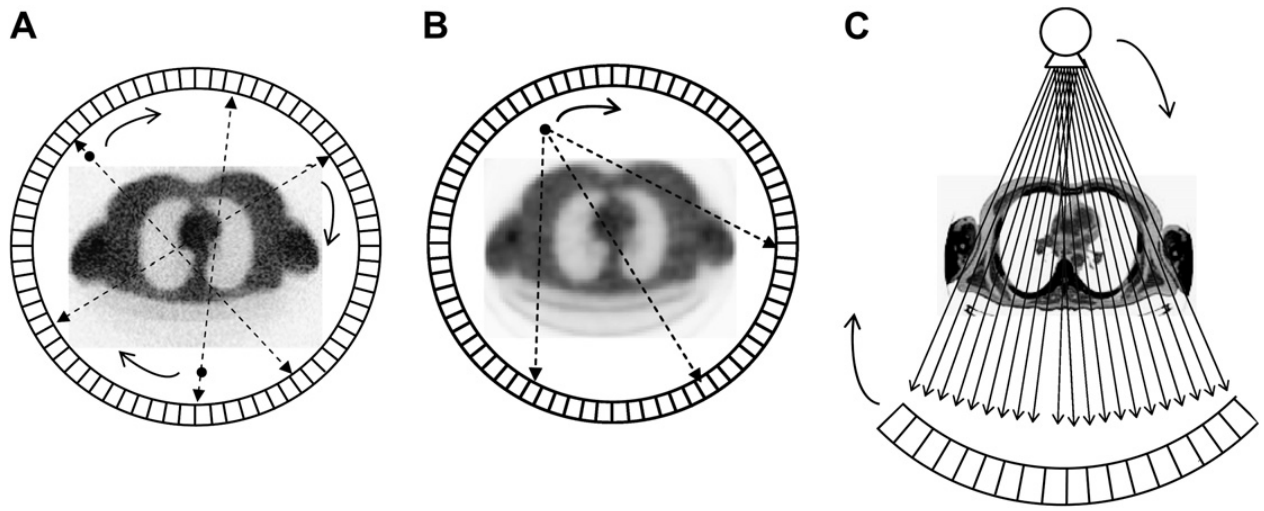

Fig. 3. Sketchy illustration of different configurations of transmission scanning geometries for positron emission tomography (PET) is shown. (*A*) rotating positron-emitting rods measuring transmission in coincidence mode. (*B*) Single-photon source producing coincidence events between the known source position and photons detected on the opposing side of the detector ring. (*C*) X-ray CT scanning using a x-ray tube and detector on the opposite side typically mounted on modern combined PET/CT scanners.

rod sources of the same radionuclide (approximately 400 MBq) [1]. The sources rotated around the edge of the field of view (FoV), recording coincidences between detectors on the near and far sides of the subject. A separate scan using the same sources is performed without the patient in the FoV. The coincidences recorded during the blank (without the object in the FoV) scan are divided by those acquired during the TX scan (with the object in the FoV) to give the ACFs for each LoR:

$$ACF = \frac{blank}{transmission} = \frac{I_0}{I_0 \exp\left(-\int\limits_{L(s,\theta)} \mu(x)dx\right)} = \exp\left(\int\limits_{L(s,\theta)} \mu(x)dx\right) \quad (3)$$

where I_0 is the blank count rate recorded at the current LoR; $\mu(x)$ is the linear attenuation coefficient at position x in the body, and $L(s,\theta)$ is the integration path along the LoR.

It might seem at first glance that the AC process is straightforward and can be performed simply by multiplying the EM projection data by the measured ACFs on a LoR-by-LoR basis. The noisy nature of TX data, however, will lead to a substantial decrease of signal-to-noise ratio (SNR) in the corrected PET data [43]. This takes place owing to the fact that the denominator in Equation 3 might be very small, either in the presence of high-density tissue, or large attenuation path length through which annihilation photons pass and because TX data obey Poisson statistics (as do all radiation EM and detection processes). One efficient way to get around this hurdle consists in low-pass filtering of TX and blank scans before computing the ACFs [5].

The rod windowing technique was developed mainly to allow postinjection TX scanning [44]. The principle is based on continuous encoding of the source location and discrimination between projection elements indicating collinear (or nearly collinear) detector pairs and those that are not. Coincidences recorded in a narrow window centered on each rod source (primarily TX events) are stored independently from those recorded outside the window (mostly EM events). Appropriate techniques were proposed to correct for EM contamination of TX measurements recorded within the window in postinjection TX scanning [45–47].

The previously described rod windowing technique was extended later on to allow simultaneous EM and TX scanning [48,49], which has the advantage to reduce substantially the acquisition time. Despite its promising features, very few centers adopted the approach for use in routine clinical whole-body PET studies [50,51]. A more elaborate approach also was proposed to reduce contamination of the EM data by the TX photons in simultaneous scanning through the use of a fast, dedicated, lutetium oxyorthosilicate (LSO)-based reference detector placed close to the collimated coincidence point source used to produce the TX data [52].

The most important drawback of positron-emitting TX sources is the high photon flux in the detectors closest to the source, which usually leads to longer scan times because of dead time. To improve counting statistics without increasing acquisition time, some investigators proposed to use single-photon emitting sources such as ^{137}Cs (662 keV, $T_{1/2}$ = 30.04 years), where LoRs are formed between

the known location of the point source as it rotates around the patient and the detector on the opposite side that absorbs the transmitted photons [53,54]. This is a more efficient approach compared with coincidence detection using positron-emitting radionuclide sources, which necessitates detection of both annihilation photons by the PET detectors. The direct consequence is a much improved SNR in ACFs generated using single-photon sources compared with those generated using positron-emitting sources [3]. An additional advantage is that single-photon sources can use isotopes that emit photons at an energy different from the 511 keV of annihilation photons (eg, ^{137}Cs), thus allowing efficient implementation of postinjection TX scanning with reduced contamination of TX images by PET data. The technique has a major drawback, however, given that the TX data need to be normalized on a daily basis (90 minutes on the ECAT ART scanner (CTI/Siemens Medical Solutions, Knoxville, Tennessee) [55]) to a slab phantom scan to correct acquired data for scatter and cross section variation using a log–linear transformation of the attenuation factors [56]. Various strategies also have been suggested to reduce contamination of EM data by TX photons for simultaneous scanning and to reduce spillover of EM data into the TX energy window [47–51]. For example, it has been demonstrated, using data from the High Resolution Research Tomograph (HRRT - Siemens Medical Solutions, Knoxville, Tennessee) brain dedicated PET scanner, that EM contamination can lead to gross underestimation of attenuation coefficients [57]. It also was reported that the most accurate way to compensate for this is to combine nonuniform EM contamination subtraction with TX image segmentation.

Segmented AC was proposed to reduce noise propagation from the short TX to the EM scans during the multiplicative AC process. This can be achieved through tissue classification schemes, which consist of delineating anatomic regions having different attenuation properties followed by assignment of known tissue-dependent attenuation coefficients using weighted averaging. The segmented attenuation maps then are forward projected to generate ACFs with reduced noise that can be used for AC of the PET data.

Clinically relevant segmentation algorithms were designed by balancing image quality and required algorithmic complexity and resulting computational time [58]. Most TX image segmentation algorithms fall into one of the following two classes: classical histogram-based adaptive thresholding techniques [59–61] and fuzzy clustering-based approached [55,62]. Adaptive thresholding-based techniques use the gray-level histogram counts to distinguish between regions. Because only intensity information is used for the segmentation, this often results in noisy segmentations, and the technique most likely fails in regions where the total number of counts is small (eg, the skull), given that the classification is based solely on the characteristics of the histogram. Therefore, the performance of such techniques strongly depends on the choice of the thresholds. On the contrary, fuzzy clustering-based segmentation techniques have proved to be more robust as automated, unsupervised algorithms for segmenting noisy images for different applications [58]. These are iterative approaches that minimize an objective function requiring the number of clusters as input parameter to assign a membership degree to all voxels with respect to a cluster center.

Other attractive approaches to segment noisy TX data include the use of active contour models [63], neural networks [64], three-dimensional edge detection techniques [65], morphologic segmentation [66], and hidden Markov modeling [67]. Alternatives to segmentation of TX images with the goal of reducing noise in PET TX measurements include Bayesian image reconstruction [68–70] and nonlinear Gaussian [71] and non-Gaussian [72] smoothing or anisotropic diffusion filtering [73].

X-ray CT-based transmission scanning

Conventional AC procedures developed for standalone PET units traditionally have been performed using external radionuclide TX sources. The procedure is conceptually analogous to the principle of x-ray CT imaging, where the radiation emanating from a rotating x-ray tube is transmitted through the patient's body and recorded by an array of detector elements on the opposite side. A tomographic reconstruction algorithm then is used to calculate the spatial distribution of attenuation coefficients. On commercial CT scanners, the reconstructed intensities usually are represented in terms of normalized (to water) CT numbers or Hounsfield units (HU), named after Godfrey Hounsfield, an established pioneer and recipient of Nobel prize in medicine (1979) for significant contributions to the development of CT [74]. Yet, the pixel values are related directly to the linear attenuation coefficient (μ) at the same point in the patient, calculated for the effective energy of the polyenergetic photon beam used to create the CT image:

$$CT\ number = \frac{\mu - \mu_{H_2O}}{\mu_{H_2O}} \times 1000 \quad (4)$$

Note that with this definition, air and water have a CT number of -1000 HU and 0 HU, respectively.

As a result, the use of low-noise x-ray CT images to create patient-specific attenuation map for correcting the PET data for photon attenuation is relatively straightforward. The technique first was explored in

the context of SPECT imaging using realigned CT data [75] and pioneered by the University of California San Francisco (UCSF) group for combined SPECT/CT imaging [76]. The same approach was investigated later by the University of Pittsburgh Medical Center group (Pittsburgh, Pennsylvania), which developed the basis of CT-based AC using sequential scanning of the patient separately on standalone PET and CT scanners followed by off-line image registration [77]. Interest in CT-AC was revived with the commercial introduction and popularity of combined PET/CT and SPECT/CT units [78]. Nevertheless, numerous pitfalls arise from the use of CT to generate attenuation maps for correction of the PET data that must be considered to avoid typical artifacts that are unique to PET/CT imaging. These are discussed further in the Pitfalls of CT-AC section.

As mentioned previously, x-ray CT inherently provides a patient-specific measurement of the electron density and thus the linear attenuation coefficient at each pixel in the CT image. Usually the high-resolution anatomic images are first downsampled, followed by Gaussian filtering to match the resolution of the PET data. The energy dependence of the attenuation coefficient is taken into account by calculating scaling factors to convert the linear attenuation coefficient at the x-ray effective energy to the 511 keV energy of annihilation photons. The most widely used calibration method is based on techniques developed for bone mineral density studies with quantitative CT. The calibration procedure begins by acquiring CT scans from a phantom containing tissue-equivalent calibration materials having known chemical compositions (Fig. 4). CT scans of the calibration phantom are acquired. Regions of interest then are defined for each compartment containing a calibration material, allowing the user to determine the mean CT number produced for each specific material. A calibration curve then is generated in which the measured CT number is plotted against the known attenuation coefficient at the photon energy of the radionuclide used in the EM study. The resulting calibration curve is piece-wise linear and covers the range of linear attenuation coefficients commonly encountered in the body. CT values below that of soft tissue (ie, water) have a slope corresponding to mixtures of soft tissue and air (eg, including those encountered in lung), while those having attenuation coefficients above water have a slope corresponding to mixtures of soft tissue and bone. The resulting calibration curve can be used to convert CT values obtained from patient scans to their equivalent linear attenuation coefficients for the desired radionuclide photon energy. Fig. 4 shows typical piece-wise calibration curve required for practical implementation of CT-AC. It should be noted that attenuation caused by Compton scatter is related to object density, whereas photoelectric absorption is related to both density and atomic number. This results in a clear distinction between soft tissue and cortical bone; the latter has more calcium and phosphorus (having higher atomic numbers). Bone has a higher photoelectric absorption cross section because of presence of calcium. Note also that at the PET energy (511 keV) almost all interactions are Compton scatter.

MRI-guided derivation of the attenuation map

The use of MRI guided attenuation correction in nuclear medicine imaging dates back to the 1990s, when the approach was investigated independently

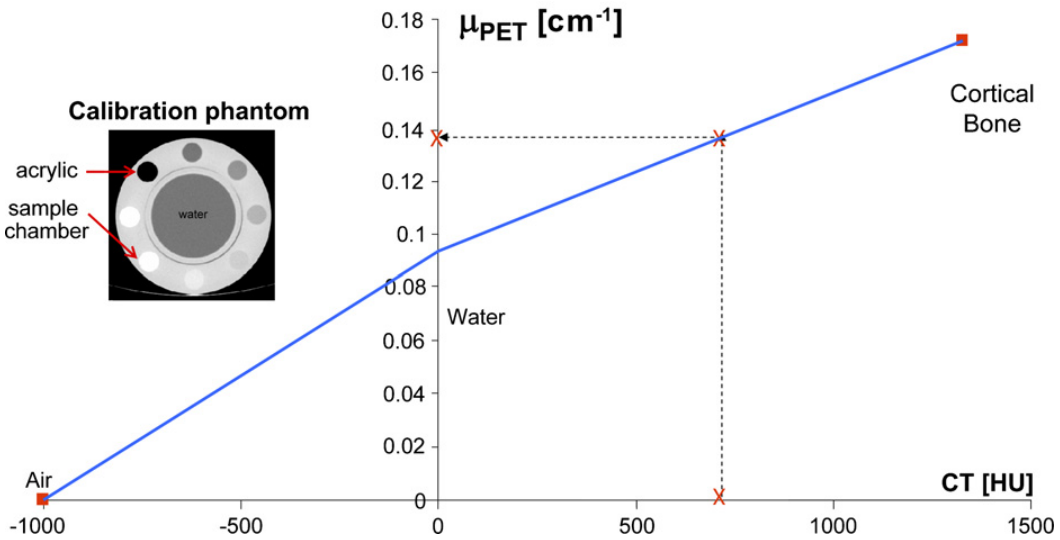

Fig. 4. Representative bilinear calibration curve determined experimentally at 120 kVp for conversion of CT numbers (HU) into linear attenuation coefficients at 511 keV. A typical polyethylene cylindric phantom containing eight cylindric holes allowing one to calibrate the CT scanner using various samples with known density and composition is shown in the upper left corner.

in the context of thoracic SPECT [79] and brain PET imaging [80]. These techniques relied on software-based image registration algorithms to realign functional and anatomic images. The recent interest and successful implementation of simultaneous PET/MRI units that can operate simultaneously (rather than sequentially as compared with PET/CT) further stimulated the development of these techniques [81].

The major difficulty facing MRI guided AC lies in the fact that the magnetic resonance signal or tissue intensity level is related directly to proton density and not to electronic density, which renders conversion of magnetic resonance images to attenuation maps less obvious compared with CT. The limited space available on PET/MRI units makes placement of external radionuclide sources difficult or even impossible. The basic problem of attenuation map determination from MRI is to locate and map the major attenuating structures in the body. Theoretically, this can be achieved in two steps: segmentation into regions of tissues/organs having different attenuating properties and assignment of corresponding linear attenuation coefficients at 511 keV to the segmented tissues/organs.

Attempts were pursued to construct a nonuniform attenuation map from MRI for brain SPECT imaging [82]. In this approach, the MRI is segmented into bone and soft tissue classes to yield a nonuniform attenuation map by modifying the uniform attenuation map to model bone of the skull by the water thickness that would result in the same attenuation (eg, μ equals 0.153 cm^{-1} at 140 keV). A nonuniform water envelope then is added to the surface of the brain to account for nonuniform bone compartment. The method, however, ignores the hollow space of sinus and air cavities that are inevitably present within the head. A more sophisticated approach for brain PET imaging based on coregistered T1 weighted three-dimensional magnetic resonance images has been proposed recently [83]. The magnetic resonance images are first realigned (after brain extraction) to preliminary reconstructions of PET data obtained using calculated AC and then segmented using a fuzzy clustering technique by identifying tissues of significantly different density and composition. The voxels belonging to different regions are classified into bone, brain tissue, and sinus cavities. These voxels then are assigned theoretic tissue-dependent attenuation coefficients as reported in the International Commission on Radiological Units and Measurements 44 report [84] and the resulting image smoothed using a Gaussian kernel. The technique was refined further by automating the segmentation of the skull procedure of T1 weighted MRI using a sequence of mathematical morphologic operations [5]. Before the segmentation of skull, the algorithm segments the scalp and the brain from the magnetic resonance image. The scalp mask allows one to quickly eliminate background voxels with intensities similar to those of the skull, while the brain mask ensures that the brain does not intersect the skull segmentation [85]. The inner and the outer skull boundaries can be computed using thresholding and morphologic closing and opening operations. The results then are masked with the scalp and brain volumes to guarantee closed and nonintersecting skull boundaries. Fig. 5 illustrates the performance of MRI-guided derivation of the attenuation map as compared with the CT-based approach for clinical brain PET imaging [5]. The figure shows the transaxial CT cross section, the corresponding coregistered MRI cross section, and the segmented MRI required to generate

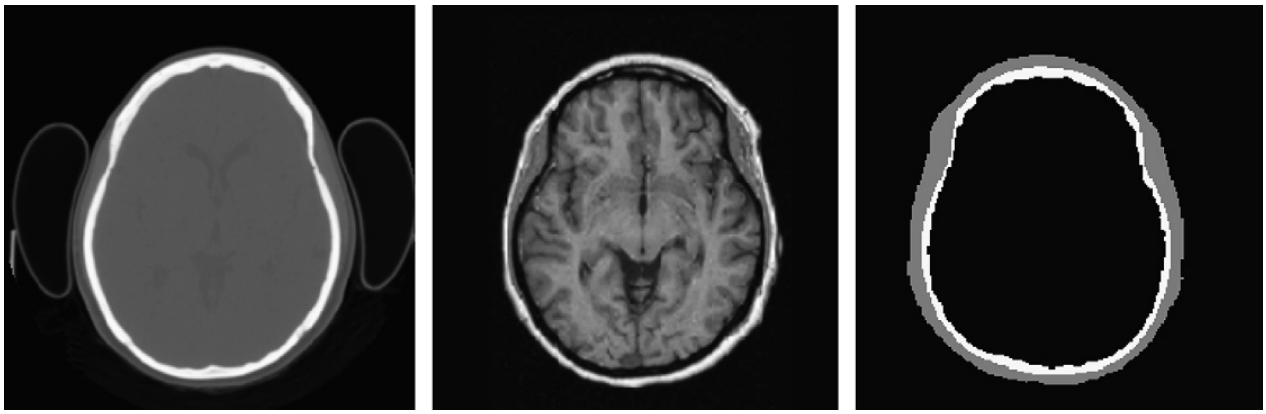

Fig. 5. Illustration of the performance of MRI-guided derivation of the attenuation map as compared with CT-based approach for clinical brain positron emission tomography (PET) imaging. From left to right: transaxial CT cross section and its corresponding coregistered MRI cross section and the segmented MRI required to generate a three-tissue compartment head model corresponding to brain, skull, and scalp. White voxels are labeled as skull; dark gray voxels are labeled as scalp, and intracranial black voxels are labeled as brain tissue. (*Reprinted from* Zaidi H, Montandon M-L, Meikle S. Strategies for attenuation compensation in neurological PET studies. Neuroimage 2007;34:518–41; with permission.)

a three-tissue compartment head model corresponding to brain, skull, and scalp using the algorithm mentioned previously [85]. Compensation for attenuation in the bed and head holder can be accomplished as discussed in Zaidi and colleagues [5] for calculated AC methods. The techniques described previously were developed originally for use on dedicated high-resolution brain PET cameras not equipped with TX scanning devices and where MRI is readily available for brain research studies [26]. The method is also useful for the simultaneous PET/MRI scanning system dedicated for brain research being developed by one scanner manufacturer [86].

Some of the problematic tissues in whole-body imaging are bone and brain skull, the lungs, and other unpredictable benign or malignant anatomic abnormalities with varying densities. Bone is intrinsically not detectable by MRI, as it provides a black or void signal, making it difficult to distinguish air from bone. In the head, however, the skull bone is covered by subcutaneous fat and encloses the brain. Incorporation of a priori anatomic knowledge allows for sufficient information to be collected to precisely segment magnetic resonance scans and thus to provide an accurate attenuation map. More sophisticated bone segmentation techniques using active shape models might help to circumvent the limitations discussed previously [87]. Ignoring bone was reported to be acceptable in the abdomen and hips [88] but certainly not in the thorax [89].

Another appealing approach for segmentation of the skull and bony structures is to use multispectral magnetic resonance data acquisition with varying contrast characteristics to provide additional information for distinguishing between different tissues. For example, T1 weighted images show better soft tissue contrast, whereas T2 weighted images show bony structures more clearly. The development of more refined magnetic resonance sequences to label the bone structure more precisely will play a significant role in novel methodological developments aiming at deriving attenuation maps from magnetic resonance images [90,91]. Careful optimization of the magnetic resonance sequences is a prerequisite for successful implementation of the technique and needs to be investigated further. Long acquisition times, however, make acquisition of more than one magnetic resonance sequence (as needed for some segmentation algorithms) almost impossible in practice. Another possibility would be to exploit the potential of rapid dual-tracer PET [92,93], where combination of fluoride (^{18}F)-PET for bone scanning with the tracer of interest (eg, ^{11}C-methionine) should allow scanning both tracers in a single acquisition. The preliminary results obtained using dynamic dual-tracer imaging with staggered injections appear to allow recovering overlapping signals through the use of information from kinetics and radioactive decay. Provided the additional absorbed dose is reasonable, the bone scan should allow—through segmentation—the mapping of bony structures in the body.

Segmentation of lung regions in thoracic MRI is another challenging issue that has received little attention owing to its limited clinical value until this modality became feasible as a result of new developments in enhanced pulse sequences, reduced scanning time, and introduction of new contrast media (eg, hyperpolarized gas) [94–97]. This has been performed, for example, through merging of multiple active contours [94], region-based segmentation [98], and edge-based and model-based techniques [99], successfully partitioning the image volumes into major anatomic structures, including lungs, heart, cardiac ventricles, and thorax outlines. Despite successful segmentation, however, a noteworthy difficulty is that some tissue regions have continuously varying densities that may not be represented correctly by a discrete set of a priori established tissue models. With respect to MRI-guided AC, the lung is one of the most challenging organs, given that it has been shown that the density of lung tissue: Is considerably different from subject to subject, depends on breathing patterns, and varies with age and in the event of respiratory diseases by as much as 30% [100].

Another approach is to use representative anatomic atlas registration, where the MRI atlas is registered to the patient's MRI, and prior knowledge of the atlas' attenuation properties (for example through coregistration to CT or TX atlas) is used to yield a patient-specific attenuation map [101]. The critical and crucial part of the algorithm is the registration procedure, which might fail in some cases with large deformations. The second fundamental question that remains to be addressed is: does the global anatomy depicted by an atlas really predict individual attenuation map? The use of support vector machines to predict the attenuation coefficients directly from the local image information by training a machine learning algorithm using small image patches has been reported recently [102]. Combination of this approach with the atlas registration described previously might be an appealing technique. Despite the remarkable results presented so far, which seem promising, more research remains needed to fully automate the procedure and to render it applicable to whole-body imaging [81]. Moreover, the clinical applicability of this approach remains to be demonstrated.

Comparison of methods

Within the context of whole-body imaging, the problems associated with the use of CT-AC on one hand and the complexity inherent to advanced

computational methods for transmissionless AC [70,103,104] spurred the further development of TX-based AC methodologies, which remain an active research area. Some scanner manufacturers decided to preserve radionuclide TX scanning devices on new-generation hybrid PET/CT units such as those implemented on the SceptreP3 (Hitachi Medical Systems America, Inc., Twinsburg, Ohio), Gemini (Philips Medical Systems, Best, The Netherlands), and also the first units of the Discovery LS PET/CT series (GE Health care Technologies, Waukesha, Wisconsin). This allows the combination of both CT and radionuclide scanning-based AC to effectively image patients with metal implants and prosthetics. A limited number of studies reported in the literature detailed comparative assessment studies between CT-AC and radionuclide scanning-based AC, including ^{68}Ga versus CT-AC [31,105–114] and ^{137}Cs versus CT-AC [115,116]. Clinical and scientific data are required to impartially establish whether the advantages and clinical benefits of TX scanning-based AC are sufficient to offset its additional running costs, or whether CT-AC should be the only option on hybrid PET/CT units [14].

It is undisputable that CT-AC has several virtues and should be targeted for further research. It should be recognized, however, that its clinical benefits have not been demonstrated unequivocally, and these benefits should be documented carefully by investigators for wider acceptance. The key point is that many PET procedures do not require a diagnostic quality CT, and radionuclide-based TX scanning would be a better option than low-dose CT protocols. It is still too early to claim that TX scanning devices are obsolete for PET/CT, and that CT-AC should be the gold standard on these systems. The authors' opinion is that TX scanning still has a genuine role and remains an appealing alternative until all the problems associated with CT-AC are resolved through research [14].

Attenuation correction strategies in positron emission tomography

The fundamental equation that links the imaged object $f(x,y)$ and corresponding attenuation map $\mu(x,y)$ to its measured projections $p(s,\theta)$ is called the attenuated Radon transform and is given in the case of PET by:

$$p(s,\theta) = \int_{L(s,\theta)} f(x,y)\, dr \times \exp\left[-\int_{L(s,\theta)} \mu(x,y)\, dl\right] dr \qquad (5)$$

where $L(s,\theta)$ is the integration path along the LoR, and θ is the angle between the rotating detector plane and the stationary reconstruction plane.

The ideal solution would have been to use an exact formula for the inverse problem to solve the Radon transform and reconstruct the spatial distribution of the tracer $f(x,y)$. Owing to the complexity of the equation in the case of nonuniform attenuation, however, an exact solution is not possible in general. The seminal contribution by Novikov [117,118], who recently gave an explicit inversion formula for the attenuated Radon transform for a particular important family of weights, was a major breakthrough in the field. Moreover, Novikov's formula was proven for a somewhat larger class of weight functions using a completely different and more straightforward method [119,120]. In spite of recent progress in the field, various approximate methods have been proposed and still are used to solve the problem of reconstructing an object from its measured projections in the presence of photon attenuation.

Measured TX scanning for AC purposes was used during the early developments of PET, which started mainly as a research tool with greater emphasis on accurate quantitative analysis. Two additional factors contributed to this logical advancement. First, AC in PET is relatively straightforward, Since in principle it requires a simple premultiplication of the measured EM data by the corresponding ACFs, and second, the ACFs in PET are large, and without AC, quantification cannot be realized.

As mentioned earlier, photon attenuation in PET is independent of the EM point along measured LoRs. In contrast, modeling the attenuation process in SPECT involves taking into account the fact that attenuation factors are dependent on the EM point, because the emitted photon crosses only part of the patient's anatomy before reaching the detector. The direct consequence is that nonuniform AC for SPECT generally requires iterative reconstruction [1].

Because AC in PET is relatively straightforward, and its accuracy is limited only by the noise (limited statistics) present in the acquired TX scans, only two techniques have materialized, and both require the computation of the ACFs through forward projection of the attenuation map at appropriate angles. To reduce processing time and data storage requirements for the three-dimensional PET data collection mode, it is often convenient to work with precorrected data. This is the basis of the first approach, where data correction is performed in projection space through multiplication of the ACFs by the measured EM data using the following expression:

$$p_{AC}(s,\theta) = ACF \times p(s,\theta) = \int_{L(s,\theta)} f(x,y)\, dr \qquad (6)$$

The attenuation-corrected projections $p_{AC}(s,\theta)$ then are used to reconstruct the images using either analytic or iterative reconstruction techniques. An attractive option is to produce a smaller set of sinograms by precorrecting the data and applying Fourier rebinning (FORE). The data, however, are no longer Poisson-distributed. It has been shown that iterative algorithms (eg, ordered subsets – expectation maximisation or OSEM) yield suboptimal images from such data [121]. Alternatively, when OSEM is used, the ACFs can be applied to provide proper statistical weighting to the data as is done in attenuation-weighted OSEM (AW-OSEM) [121]. This latter technique has better noise properties and now is incorporated in commercial software used routinely in many clinical PET facilities. For instance, it has been shown that the FORE+AW-OSEM algorithm results in the best overall detection and localization performance for 1 cm diameter lesions compared with FORE+OSEM and FORE+FBP algorithms in PET imaging [122].

Attenuation correction in small animal positron emission tomography

The demand for functional, metabolic, and molecular imaging of small animals, including mice, rats, small primates, and other mammalian species, has stimulated the development of dedicated small-bore high-resolution PET systems that contribute unique information that is becoming relevant for biomedical research [123]. Similar to scatter modeling and correction [2], little has been published on AC in small animal PET scanners owing to the low magnitude of attenuation factors (compared with clinical imaging) when imaging rodents. The magnitude of the correction factors ranges from approximately 45 for a 40 cm diameter human subject and decreases down to 1.6 for a 5 cm diameter rat) to nearly 1.3 for a 3 cm diameter mouse [124]. This elucidates why the problem of photon attenuation is small animal imaging has been overlooked even in the third generation of preclinical PET scanners [125]. PET scanner calibration factors usually are determined with and without AC, given that AC still is not well established in small animal imaging.

Fahey and colleagues [126] have shown that the use of TX-based AC improved the quantitative accuracy but also reduced the precision as indicated in the variability of the attenuation corrected data. As stated previously, this can be compensated by noise reduction schemes such as segmentation of the TX data. Another study compared several measured TX-based techniques for deriving the attenuation map on the micro-PET Focus 220 animal scanner (Siemens Preclinical Solutions, Knoxville, Tennessee) [127]. This includes coincidence mode with and without rod windowing, singles mode with two different TX sources (^{68}Ge and ^{57}Co), and postinjection TX scanning. Moreover, the efficiency of TX image segmentation and the propagation of TX bias and noise into the emission images were examined. It was concluded that ^{57}Co-based AC provides the most accurate attenuation map having the highest SNR. Single-photon TX scanning using ^{68}Ge sources suffered from degradations resulting from object Compton scatter. Monte Carlo simulation studies also demonstrated that background contamination in the ^{68}Ge singles-mode data caused by intrinsic ^{176}Lu radioactivity present in the detector crystals can be compensated for by using a simple technique [128]. Compensating for scatter improved the accuracy for a cylindric phantom approximately 10 cm diameter) but overcorrected for attenuation for a mouse phantom. Low-energy ^{57}Co-based AC also resulted in low bias and noise in postinjection TX scanning for activities in the FoV up to 20 MBq. Attenuation map segmentation was most successful using ^{57}Co single-photon sources; however, the modest improvement in quantitative accuracy and SNR may not rationalize its use, particularly for small animals. More sophisticated techniques using multiple sources for TX scanning where each point source is surrounded by a plastic scintillator coupled to a miniature photomultiplier tube to allow collection of the energy the positron must lose before annihilation also were developed. [129,130] also were developed. The LoR joining the current source position and detector position are identified through the pulse provided by the energy lost in the plastic scintillator, whereas scanner's conventional detectors provide the second pulse.

The potential use of small-animal CT for AC is established and considered to be one of the potential applications of low-dose micro-CT imaging that can drive the further development of dual-modality small animal PET/CT [131]. Similar to SPECT/CT [132,133], the accuracy of CT-AC in preclinical imaging was demonstrated using phantom and animal studies, where the low-dose CT was suitable for both PET data correction and PET tracer localization [124]. Noise analysis in phantom studies with the TX-based method showed that noise in the TX data increases the noise in the corrected PET emission data, whereas the CT-based method was accurate and resulted in less noisy images. For small animal imaging, hardware image registration approaches that rely on the use of custom made imaging chambers that can be mounted rigidly and reproducibly on separate PET and CT preclinical scanners [134] is a reasonable alternative to combined PET/CT designs [135–137]. Calculated AC was reported to provide similar correction

compared with CT-AC for a cylindric phantom and a mouse for which the attenuation medium volume matches the PET emission source distribution [138]. It undercorrects for attenuation, however, when the EM image outline underestimates the attenuation medium volume (unmatched source distribution and attenuation medium).

Pitfalls of CT-based attenuation correction in positron emission tomography and potential solutions

The progress in CT-AC methodology has been immense in the last few years, the main opportunities arising from the development of both optimized scanning protocols and innovative and faster image processing algorithms. This has permitted the implementation of much more ambitious algorithms that tackle the challenges of whole-body imaging using PET. Some solutions recently were proposed and used successfully in clinical and research settings. These include optimized contrast-enhanced CT protocols [139,140], respiratory motion compensation [39,141–143], metal artifacts reduction [144–165], truncation artifacts correction [166–170], beam hardening correction [171,172], and x-ray scatter compensation in CT [173–176]. These hot topics are discussed in the following section, and in the authors' opinion undoubtedly still require further research and development efforts.

Artifacts resulting from polychromaticity of x-ray photons and beam hardening

The x-ray beam used in CT is polyenergetic, rather than monoenergetic, as is the case for photons emitted by radionuclide TX sources. The linear attenuation coefficient measured with CT is calculated at the effective energy of the x-ray beam rather than at the energy of the annihilation photons emitted by the positron-emitting radiopharmaceutical during the emission study. A precise conversion of CT numbers derived from low-energy polychromatic x-ray spectra to linear attenuation coefficients at 511 keV is thus essential. Several strategies have been devised for calibrating the CT image for AC of the PET data, including scaling [177], segmentation [4], hybrid segmentation/scaling [77], piece-wise linear scaling [109,178], and dual-energy decomposition methods [179,180]. The dual-energy x-ray method requires acquisition of two CT scans from the same regions at different x-ray energies, which are combined to generate accurate attenuation coefficients at any desired photon energy. The technique seems promising, particularly with the development of dual-source x-ray CT scanners [181] and the introduction of dose-reduction CT scanning protocols [182,183]. It should be noted that most commercial PET/CT scanners use the bilinear calibration curve method, which generally is calculated at a preset tube voltage (eg, 120 to 140 kVp) and tube current. The effect of tube current [105,184] and tube voltage [185] on the accuracy of CT-AC has been found to be relatively small. The last reference demonstrated that the use of a single calibration curve acquired under standard imaging conditions does not affect to a visible or measurable extent neurologic PET images reconstructed using CT-AC when CT images are acquired in different tube voltages [185]. The situation is different for whole-body scanning, where calibration factors must be calculated separately for each kVp-setting at which the CT scanner is operated [186].

On the other hand, the polychromatic nature of CT and the energy-dependent attenuation of most materials make CT subject to beam hardening artifacts caused by the preferential absorption of lower-energy photons as they pass through the patient's body [187,188]. Therefore, the mean energy of the x-ray beam is higher in thick patient regions than in thin patient regions. Correspondingly, the linear attenuation coefficient calculated for thick body regions is lower than in thin regions. The consequence is that Beer's law is no longer valid, and therefore errors will propagate in the measured line integrals of the attenuation map. This can cause cupping artifacts induced by nonlinearities in the projection data that generally are corrected in the calibration software implemented as part of the standard CT reconstruction software of commercial scanners. More sophisticated beam hardening correction strategies with varying degrees of success have been proposed in the literature [159,171,172,188–190]. The field remains open for further developments.

Artifacts resulting from misregistration between emission and transmission data

The advantages and drawbacks of hardware integration versus software registration in dual-modality imaging still are being debated even one decade following the introduction of combined PET/CT in clinical routine [191–195]. Notwithstanding the success and widespread clinical adoption of PET/CT, there are several challenges that still are facing the use of dual-modality imaging, and that represent inherent limitations in this technique. One of the most significant challenges of PET/CT is the difficulty to achieve accurate registration of both imaging modalities in the presence of motion [196]. It has been advocated that software-based registration might play a complementary role when using hybrid PET/CT to offset inherent patient motion [197].

Despite much worthwhile research performed during the last few years, artifacts induced by respiratory and cardiac motion remain among the most

difficult problems to solve [196,198]. This probable trouble arises when the patient moves either voluntarily or involuntarily between or during the CT and PET data acquisitions. This might take place, for instance, if the patient changes his position while lying on the patient bed. Patient motion also might occur due to respiration, cardiac motion, peristalsis, and bladder filling, all of which can lead to motion blurring or misregistration errors between PET and CT data [199,200].

Diagnostic-quality CT data usually are acquired using a breath-hold protocol, whereas PET data are acquired over several minutes with the patient breathing softly. Differences between PET and CT breathing protocols might lead to misalignment artifacts owing to anatomic dislocations of the diaphragm and chest wall during a PET/CT scan. A slight displacement of the diaphragm's position on the CT scan can cause a substantial bias in the estimation of the tracer concentration in the reconstructed PET data when the former is used for AC [39,201]. The outcome of an inconsistency in diaphragmatic location between PET and CT is frequently the appearance of the so-called cold artifact at the lung base, which is illustrated in Fig. 6 for data acquired on the Biograph Sensation 16 PET/CT scanner (Siemens Medical Solutions, Erlangen, Germany). Many studies reported significant misalignment between the CT and the PET data. For example, in a study of 300 clinical PET/CT studies with proven liver lesions; approximately 2% appeared to have the lesion localized in the lung [202], whereas the misalignment between PET and CT data was greater than 2 cm in 34 of 100 patient studies because of respiratory motion [39].

The impact of respiratory motion has been investigated extensively in the context of oncologic PET imaging [35,37–42,141,202–209]. It has been reported that motion-induced artifacts also might affect the appearance of upper abdomen lesions, thus resulting in false-negative interpretation of liver dome lesions [115,210]. Caution therefore is recommended when reading PET/CT scans of patients suffering from disease in the periphery of the lung, where noticeable tracer uptake can be the result of respiratory motion rather than disease. Modern PET/CT scanners are equipped with helical CT technology, allowing one to acquire high-resolution anatomic images within a few seconds following patient positioning and definition of the axial FoV on the topogram. It is therefore obvious that PET is the limiting factor when it comes to scanning speed on combined PET/CT. Whenever faster scanning times are sought, PET is the imaging modality requiring improvement through the development of novel detector technologies, faster scintillation crystals and electronic boards, new geometries offering higher sensitivity, and many other means that are being explored. One possibility would be to substitute conventional PET detector blocks with LSO panel detectors [211] covering a larger axial FoV with the aim of achieving faster scan times than are achievable with current systems. In any case, faster scan times improve patient comfort and reduce the time during which patient motion can occur. Likewise, faster scan times can increase patient throughput and thereby boost system use and improve cost-effectiveness.

As an alternative, many potential solutions have been suggested to accommodate differences between breathing patterns, including retrospective AC using free-breathing CT [212], the use of optimal CT acquisition protocols [213,214], respiratory averaged CT [34,39,41,42], phased CT acquisitions [141], cine CT acquisition [215], respiratory correlated acquisitions [38,216,217], deep-inspiration breath-hold acquisition [209,218], and the use of respiratory-gated PET/CT acquisitions [196,198,204–208,219–221]. Fig. 7 shows the principle of respiratory-averaged CT (ACT), which consists of averaging 10 phases of the four-dimensional CT data sets or averaging the images from a breathing cycle to match the temporal resolutions of the CT and the PET data. The technique offers significant advantages compared with helical CT (HCT) and enhances significantly the observed tracer uptake in pulmonary lesions. Fig. 8 illustrates an example of registration error caused by an undercorrection of attenuation by HCT [41]. The HCT and ACT images are shown in (A) and (B), respectively. The region of mismatch was derived from the difference image (E) between the PET data corrected with ACT (D) and the PET data corrected with HCT (C). The region of difference in quantification corresponds to the difference in the lateral walls between the HCT and the ACT data. This example emphasizes the importance of registration between the PET and the CT data to ensure an accurate quantification of the myocardium data in PET/CT imaging [41]. Cardiac motion also can be a source of misregistration between the CT and PET images and has been described extensively in the literature [29–34,112,214,215,222,223]. Similar findings have been reported using combined SPECT/CT units [224–227].

Artifacts arising from the use of contrast-enhanced CT

Owing to its low sensitivity, perfusion is the only in vivo functional information provided by CT in contrast-enhanced studies. On the basis of published literature, the authors understand that the use of contrast-enhanced CT in connection with PET/CT imaging remains subject to controversy

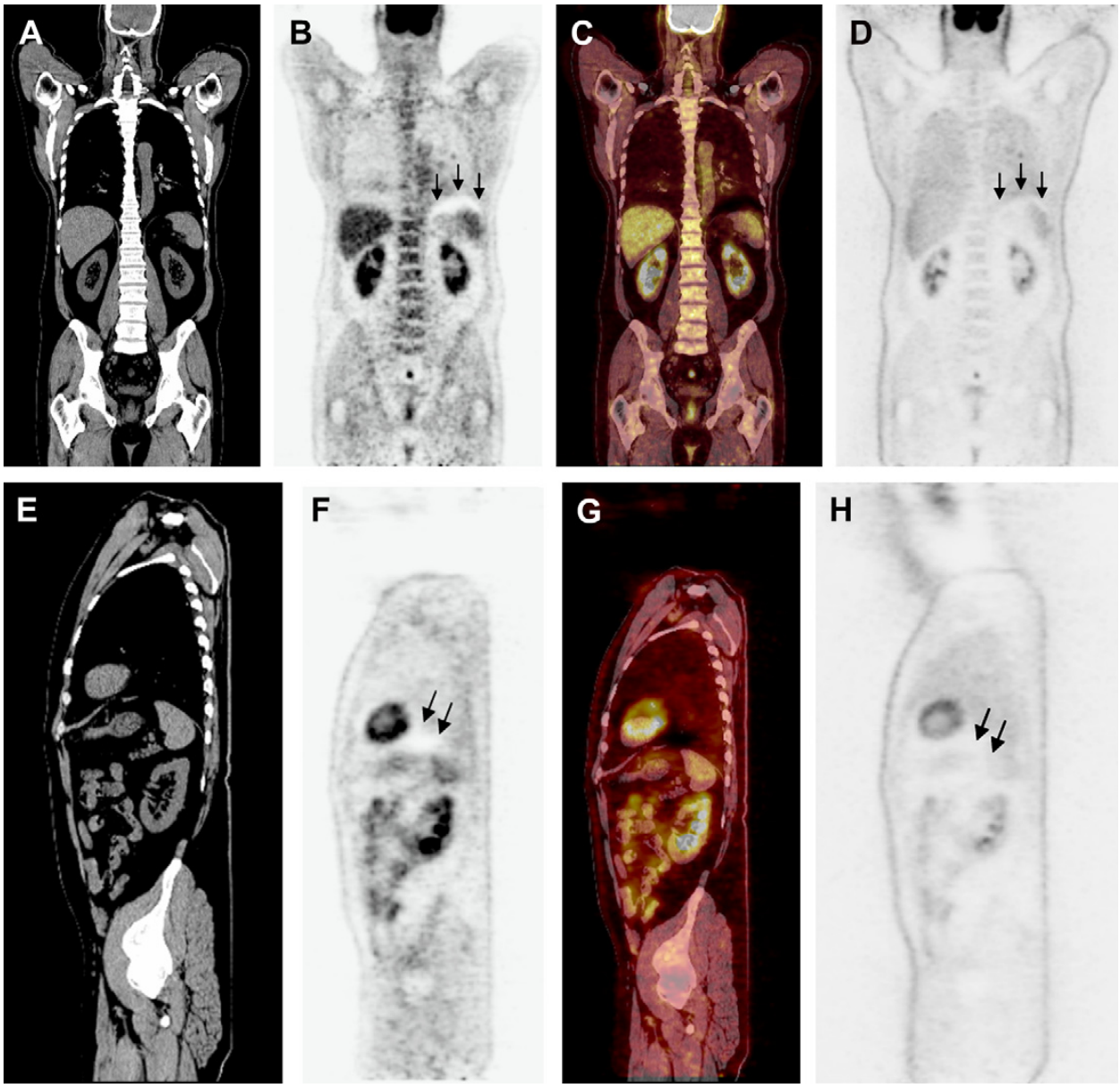

Fig. 6. Illustration of a respiratory motion related artifact on positron emission tomography (PET) images reconstructed with CT-based attenuation correction. (*A*) Coronal CT, (*B*) coronal attenuation corrected ^{18}F-FDG PET, (*C*) coronal fused PET/CT image, (*D*) coronal nonattenuation corrected ^{18}F-FDG PET, (*E*) sagittal CT, (*F*) sagittal attenuation corrected ^{18}F-FDG PET, (*G*) sagittal fused PET/CT image, (*H*) sagittal nonattenuation corrected ^{18}F-FDG PET. A region of decreased metabolic activity is demonstrated in the diaphragmatic region (*vertical arrow*), representing a cold artifact. Note that this artifact is not apparent on the noncorrected image.

[228–237]. Diagnostic-quality CT, however, generally dictates the administration of either intravenous or oral contrast, or both as in the case of lymphoma studies, and the use of high current, to provide high-quality diagnostic CT studies. Recent studies seem to suggest that contrast-enhanced CT might not be needed in many indications including Hodgkin's disease and non-Hodgkin's lymphoma [238,239], whereas it is advised strongly in staging and therapy planning in nonsmall cell lung cancer [236].

The concern of whether the use of contrast medium in dual-modality PET/CT imaging produces medically significant artifacts remains controversial, with some studies corroborating [176,228,240,241] and others contradicting [231–233,242,243] the fact that the presence of contrast medium can be a source of errors and artifact when the CT data are used for attenuation correction of PET images depending on the route of administration and phase protocol of CT imaging [140]. The optimal quantity and route of administration of contrast medium and potential correction schemes remain open questions that require further research and development efforts [139]. Other strategies include the acquisition of precontrast and postcontrast CT scans that can be used to minimize possible artifacts contributed by the presence of contrast media when

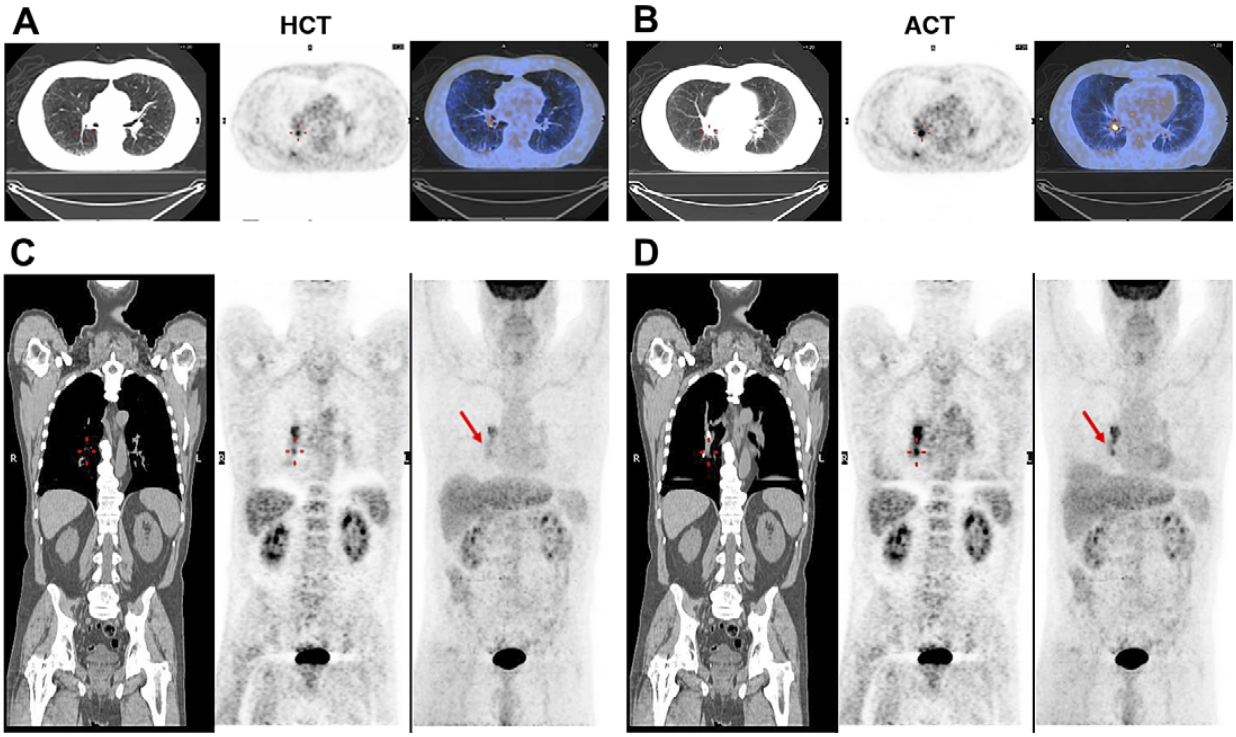

Fig. 7. (*A*) Axial helical CT (HCT) and positron emission tomography (PET) data (corrected by HCT) for a clinical PET/CT study. (*B*) Corresponding axial respiration-averaged CT (ACT) and PET data (corrected by ACT). To enhance interpretation, both HCT and ACT images are shown with CT level of -700 and window width of 1000. SUV for HCT PET and ACT PET were 4.3 and 7.4, respectively. SUV increased 70.1% from HCT PET to ACT PET. (*C*) Coronal HCT, HCT PET, and maximum-intensity projection (MIP) of HCT PET data. (*D*) Coronal ACT, ACT PET, and MIP of ACT PET data. With ACT, there was a significant reduction in breathing artifacts caused by different breathing states during HCT and PET. Note that ACT did not cover whole lung and was still able to correct for breathing artifacts. On each image, crosshair or arrow indicates tumor location. (*Reprinted from* Pan T, Mawlawi O, Nehmeh SA, et al. Attenuation correction of PET images with respiration-averaged CT images in PET/CT. J Nucl Med 2005;46:1481–7; with permission.)

the CT scan is to be used as an attenuation map for correction of the PET data. As a rule of thumb, examination of the uncorrected images is recommended to distinguish technical artifacts from physiologic/pathologic hypermetabolism.

Various techniques were suggested to correct for the presence of oral [242,244–246] and intravenous [176,247,248] contrast agents in whole-body PET/CT, including cardiac PET/CT [249]. The segmented contrast correction (SCC) method originally proposed by Nehmeh and colleagues [242] consists of identifying through manual segmentation the regions that contain contrast medium and then substitute the CT numbers of pixels belonging to these regions with their equivalent effective bone CT numbers, because the commonly used bilinear calibration curve is derived based on the assumption that positive CT numbers are contributed by a mixture of tissue and bone. The technique later was extended to be applicable to intravenous contrast agents [176]. The technique was evaluated using phantom and clinical studies and proved to accurately recover lesion size and uptake. One of the drawbacks of this technique is the limited scope of possible applications given that the enhanced regions reflecting the spatial distribution of contrast medium are limited to simple geometric shapes. This limitation renders the algorithm of limited value in clinical settings where the shapes encountered are rather irregular. The problem arises from the difficulty in appropriately segmenting and classifying bone and contrast-enhanced fluids (CEF) in patient's CT images. More recently, an automated algorithm for segmentation and classification of irregular shapes of regions containing contrast medium usually found in clinical CT images was proposed for wider applicability of the SCC algorithm for correction of oral contrast artifacts [246]. Fig. 9 shows a clinical PET/CT study deemed to be problematic to demonstrate the applicability of the previously referenced automated segmentation technique in a clinical environment. The patient previously had oral barium administration for esophageal, gastric, and duodenal transit assessment, which was known to remain in the abdomen during the PET/CT scan. It can be seen that the correction of oral contrast artifacts improves the readability and interpretation

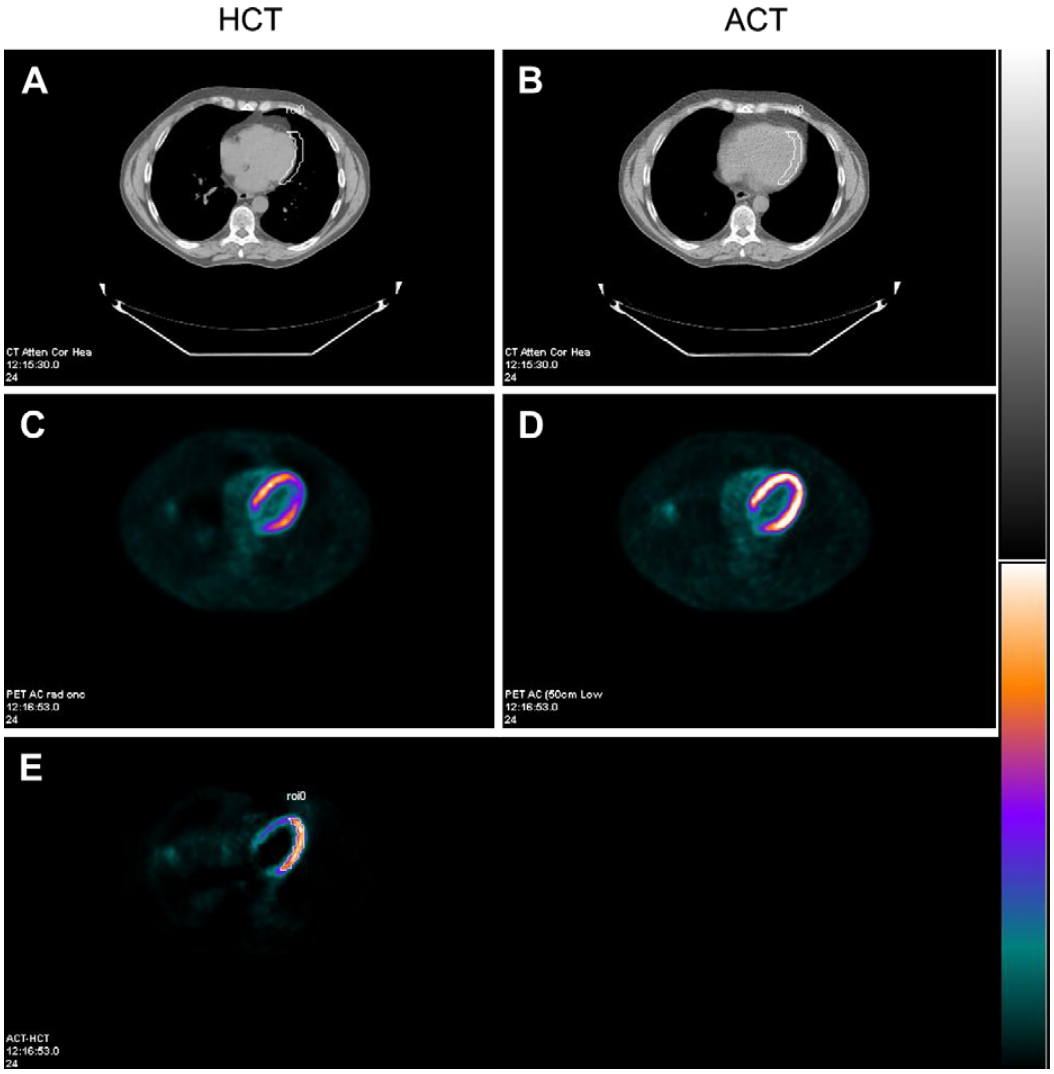

Fig. 8. Illustration of the difference in quantification of the positron emission tomography (PET) data in (*E*) between the PET data in (*C*), corrected with the axial helical CT HCT data in (*A*), and the PET data in (*D*) corrected with the ACT data in (*B*). A segmented region in (*E*) also is duplicated in the HCT data in (*A*) and the ACT data in (*B*). This example demonstrates the cause of misregistration when a part of the lateral walls of myocardium in the PET data are attenuation corrected with the lower attenuation of the lungs when they should have been corrected with the higher attenuation of the heart tissues. (*Reprinted from* Pan T, Mawlawi O, Luo D, et al. Attenuation correction of PET cardiac data with low-dose average CT in PET/CT. Med Phys 2006;33:3931–8; with permission.)

of the PET scan and shows substantial decrease of the SUV (104.3%) in the region containing contrast medium after correction [246].

Truncation artifacts

Truncation artifacts occur when there is a discrepancy between PET and CT fields of view in a combined PET/CT scanner. In most commercial designs, the FoV of the CT component usually is truncated to 50 cm, whereas the PET FoV may extend up to 70 cm. Truncation artifacts potentially occur when scanning extends beyond the CT FoV, which might happen frequently when scanning obese patients. It is also very common to extend the CT FoV to 70 cm through analytic extrapolation of the projection. This might increase the bias introduced into the PET data through the CT-AC procedure, however. Few studies focused on the assessment of the impact of artifacts resulting from truncation of CT images, particularly on tracer activity concentrations in clinical oncology resulting in the proposal of various strategies for truncation correction [166–170]. In most of the cases, an extended FoV algorithm is used to estimate complete unmeasured projections outside the CT FoV from nonlinear extrapolation of the truncated projections. Performance assessment of algorithms usually is performed by comparing PET tracer distribution and uptake obtained through reconstructions using CT images reconstructed from truncated and extended projections, respectively. It has been shown that truncation artifacts in whole-body PET/CT lead to

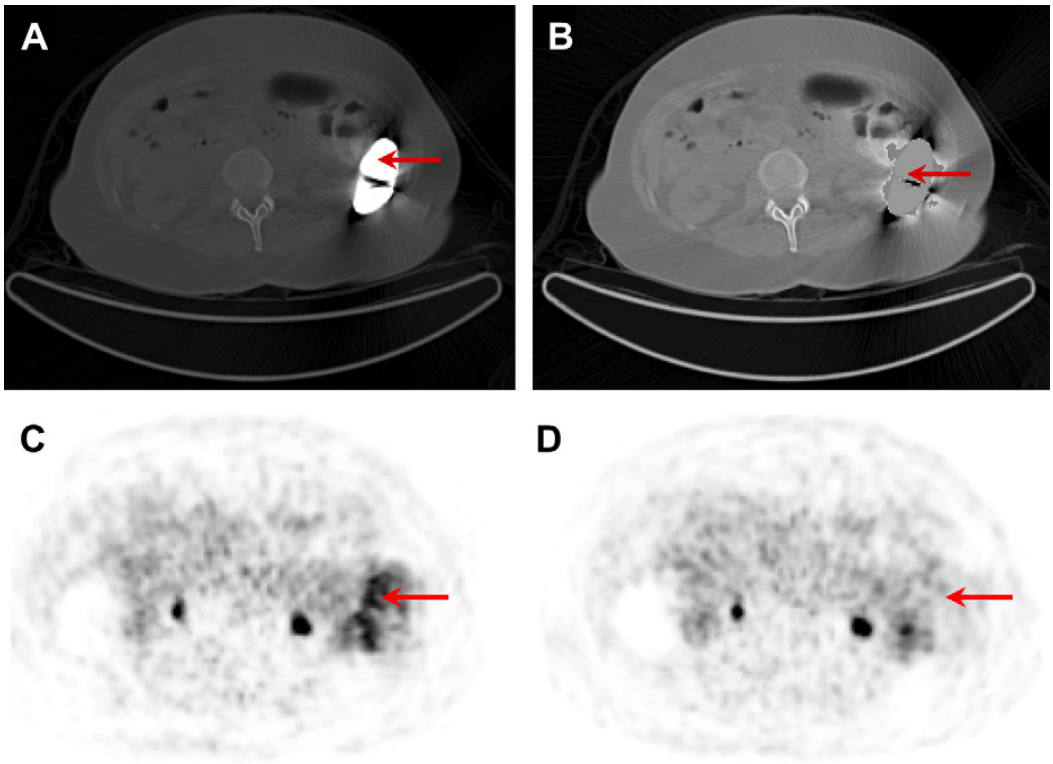

Fig. 9. Transaxial slices of generated CT-based attenuation maps before (*A*) and after (*B*) correction of oral contrast-related artifacts using an automated segmentation algorithm and corresponding positron emission tomography (PET) images (*C* and *D*) reconstructed using the attenuation maps shown in (*A*) and (*B*), respectively. Note the contrast-related artifacts (*arrows*).

visual and quantitative distortions of the CT and attenuation-corrected PET images in the area of truncation [166–168]. Truncation correction algorithms allow one not only to achieve artifact-free images in the FoV but also to extend the images beyond the FoV, and these algorithms should be applied when available.

Artifacts arising from metallic objects

The presence of metallic objects is a major problem in CT, as they tend to generate strong artifacts in reconstructed CT images owing to the presence of strongly attenuating objects in the FoV. The presence of metallic dental implants [250,251] or electroencephalogram (EEG) electrodes [165] typically used for monitoring epilepsy patients can introduce visible artifacts into brain images when CT is used to determine the attenuation map in PET/CT. Similar observations have been made for metallic hip prosthetic material [252,253] and pacemakers [160,254,255]. The most important causes of metal artifacts are noise, beam hardening, the non-linear partial volume effect, and scatter.

The maximum voxel intensity in reconstructed CT images is 3071 HU on virtually all clinical CT scanners except when an extended CT scale is used [256]. The consequence is that metallic objects will be assigned this maximum value, which obviously underestimates their true HU. Even when the extended CT scale is used, however, currently available conversion methods likely will undercorrect for attenuation of metallic objects. When the obtained CT data are used for AC of the corresponding PET emission data, LoRs passing through metallic objects will be assigned wrong ACFs [165].

The general hypothesis lying behind the development of metal artifact reduction algorithms is that the artifacts are caused by deviations of the acquisition model assumed by the reconstruction from the true acquisition process. Consequently, improving the acquisition model should reduce artifacts. Various metal artifact reduction (MAR) algorithms have been suggested in the literature [110, 144–165,184,254,255,257–259]. For example, the MAR algorithm proposed in by Lemmens and colleagues [161,165] starts with an initial reconstruction performed using an iterative ML algorithm for transmission tomography (MLTR) [158]. This initial image estimate is used to produce a label image on which multimodal priors are defined [70]. A maximum-a-posteriori (MAP) reconstruction then is performed using these priors to obtain an artifact-free starting image [260]. This starting image serves as the basis for an image-based projection completion procedure, where the measured metal

projections are substituted by artificially computed projections. The final step of the algorithm consists in performing the final reconstruction through the use of the corrected dataset and MLTR.

Artifacts arising from x-ray scatter in CT images

A limited number of studies have investigated the magnitude and spatial distribution of the scatter component in radionuclide TX scanning [261,262]. Historically, the scatter component was assessed extensively in the context of quantitative CT imaging [189,263–265]. Interest in scatter characterization and correction in CT images was revived following the introduction of PET/CT and the successful implementation of CT-AC procedures. The scatter component in CT data was assessed both in fan beam [189,263–265] and cone beam [173,175,266–269], including flat-panel [174–176, 270–274] geometries. This is discussed in detail in the article by Zaidi and Montanden in this special issue [2].

Summary

High-resolution cutting-edge PET and PET/CT technology is poised to advance the understanding of human disease complexity and improve the clinical management of patients through translational research. The hope is to be able to provide predictive, preventative, and personalized medicine that is expected to radically transform the practice of medicine and shift in health care. This only can be achieved using quantitative molecular imaging, which provides accurate measures of biological processes in vivo using the most advanced PET data correction and reconstruction algorithms available today. AC is one of the most pertinent corrections that needs to be performed to get reliable results. The ability to accurately carry out AC with validated hardware/software solutions, combined with the use of rigorous quality control measures, enhances the interpretive confidence and accuracy of molecular PET imaging. Consequently, there has been growing clinical acceptance of the need to systematically perform AC in clinical setting following its successful implementation in research environments. Postinjection TX scanning remains the most widely used method on standalone PET units, although this is changing rapidly with the introduction of dual-modality PET/CT systems, where CT-AC was imposed as the new gold standard despite the many problems discussed in this article [14]. The development of suitable AC strategies on novel dual-modality imaging technologies such as PET/MR remains challenging and will attract the interest of active researchers in the field in the foreseeable future [81].

Despite the remarkable progress in AC achieved during the last decade, there is still scope for further research to address the challenges of novel techniques and stringent demands of diagnostic molecular imaging. There is every reason to believe the field will move forward more rapidly in the near future with the advent of better computing power and the unlimited imagination of researchers in the field. There is no shortage of challenges and opportunities, as the field is very open to future novel ideas (hardware, and especially software) aimed at improving the quantitative capabilities of molecular imaging techniques.

References

[1] Zaidi H, Hasegawa BH. Determination of the attenuation map in emission tomography. J Nucl Med 2003;44:291–315.
[2] Zaidi H, Montandon M. Scatter compensation techniques in PET. PET Clinics, in press.
[3] Bailey DL. Transmission scanning in emission tomography. Eur J Nucl Med 1998;25:774–87.
[4] Kinahan PE, Hasegawa BH, Beyer T. x-ray-based attenuation correction for positron emission tomography/computed tomography scanners. Semin Nucl Med 2003;33:166–79.
[5] Zaidi H, Montandon M-L, Meikle S. Strategies for attenuation compensation in neurological PET studies. Neuroimage 2007;34:518–41.
[6] Huang SC, Hoffman EJ, Phelps ME, et al. Quantitation in positron emission computed tomography: 2. Effects of inaccurate attenuation correction. J Comput Assist Tomogr 1979;3: 804–14.
[7] Ficaro EP. Should SPET attenuation correction be more widely employed in routine clinical practice? For. Eur J Nucl Med 2002;29:409–12.
[8] Wackers FJT. Should SPECT attenuation correction be more widely employed in routine clinical practice? Against. Eur J Nucl Med 2002;29: 412–5.
[9] Heller GV, Links J, Bateman TM, et al. American Society of Nuclear Cardiology and Society of Nuclear Medicine joint position statement: attenuation correction of myocardial perfusion SPECT scintigraphy. J Nucl Cardiol 2004;11: 229–30.
[10] Garcia EV. SPECT attenuation correction: an essential tool to realize nuclear cardiology's manifest destiny. J Nucl Cardiol 2007;14:16–24.
[11] Wahl RL. To AC or not to AC: that is the question. J Nucl Med 1999;40:2025–8.
[12] Bai C, Kinahan PE, Brasse D, et al. An analytic study of the effects of attenuation on tumor detection in whole-body PET oncology imaging. J Nucl Med 2003;44:1855–61.
[13] Zaidi H, Sossi V. Correction for image degrading factors is essential for accurate

quantification of brain function using PET. Med Phys 2004;31:423–6.
[14] Zaidi H. Is radionuclide transmission scanning obsolete for dual-modality PET/CT systems? Eur J Nucl Med Mol Imaging 2007;34:815–8.
[15] Bengel FM, Ziegler SI, Avril N, et al. Whole-body positron emission tomography in clinical oncology: comparison between attenuation-corrected and uncorrected images. Eur J Nucl Med 1997;24:1091–8.
[16] Bedigian MP, Benard F, Smith RJ, et al. Whole-body positron emission tomography for oncology imaging using singles transmission scanning with segmentation and ordered subsets–expectation maximization (OS-EM) reconstruction. Eur J Nucl Med 1998;25:659–61.
[17] Bleckmann C, Dose J, Bohuslavizki KH, et al. Effect of attenuation correction on lesion detectability in FDG PET of breast cancer. J Nucl Med 1999;40:2021–4.
[18] Farquhar TH, Llacer J, Hoh CK, et al. ROC and localization ROC analyses of lesion detection in whole-body FDG PET: effects of acquisition mode, attenuation correction, and reconstruction algorithm. J Nucl Med 1999; 40:2043–52.
[19] Lonneux M, Borbath I, Bol A, et al. Attenuation correction in whole-body FDG oncological studies: the role of statistical reconstruction. Eur J Nucl Med 1999;26:591–8.
[20] Weber WA, Neverve J, Sklarek J, et al. Imaging of lung cancer with fluorine-18 fluorodeoxyglucose: comparison of a dual-head gamma camera in coincidence mode with a full-ring positron emission tomography system. Eur J Nucl Med 1999;26:388–95.
[21] Hustinx R, Dolin RJ, Benard F, et al. Impact of attenuation correction on the accuracy of FDG-PET in patients with abdominal tumors: a free-response ROC analysis. Eur J Nucl Med 2000;27:1365–71.
[22] Delbeke D, Martin WH, Patton JA, et al. Value of iterative reconstruction, attenuation correction, and image fusion in the interpretation of FDG PET images with an integrated dual-head coincidence camera and x-ray-based attenuation maps. Radiology 2001;218:163–71.
[23] Maintas D, Houzard C, Ksyar R, et al. Is nonattenuation-corrected PET inferior to body attenuation-corrected PET or PET/CT in lung cancer? Nucl Instr Meth A 2006;569:167–70.
[24] Reinhardt MJ, Wiethoelter N, Matthies A, et al. PET recognition of pulmonary metastases on PET/CT imaging: impact of attenuation-corrected and nonattenuation-corrected PET images. Eur J Nucl Med Mol Imaging 2006;33:134–9.
[25] Nuyts J, Stroobants S, Dupont P, et al. Reducing loss of image quality because of the attenuation artifact in uncorrected PET whole-body images. J Nucl Med 2002;43:1054–62.
[26] Braem A, Chamizo Llatas M, Chesi E, et al. Feasibility of a novel design of high-resolution parallax-free Compton-enhanced PET scanner dedicated to brain research. Phys Med Biol 2004;49:2547–62.
[27] van den Heuvel OA, Boellaard R, Veltman DJ, et al. Attenuation correction of PET activation studies in the presence of task-related motion. Neuroimage 2003;19:1501–9.
[28] Zaidi H, Montandon M-L, Slosman DO. Attenuation compensation in cerebral 3D PET: effect of the attenuation map on absolute and relative quantitation. Eur J Nucl Med Mol Imaging 2004;31:52–63.
[29] Bacharach SL, Buvat I. Attenuation correction in cardiac positron emission tomography and single-photon emission computed tomography. J Nucl Cardiol 1995;2:246–55.
[30] Loghin C, Sdringola S, Gould KL. Common artifacts in PET myocardial perfusion images due to attenuation–emission misregistration: clinical significance, causes, and solutions. J Nucl Med 2004;45:1029–39.
[31] Souvatzoglou M, Bengel F, Busch R, et al. Attenuation correction in cardiac PET/CT with three different CT protocols: a comparison with conventional PET. Eur J Nucl Med Mol Imaging 2007;34:1991–2000.
[32] Lautamaki R, Brown TL, Merrill J, et al. CT-based attenuation correction in (82)Rb-myocardial perfusion PET-CT: incidence of misalignment and effect on regional tracer distribution. Eur J Nucl Med Mol Imaging, 2008; in press.
[33] Gould KL, Pan T, Loghin C, et al. Frequent diagnostic errors in cardiac PET/CT due to misregistration of CT attenuation and emission PET images: a definitive analysis of causes, consequences, and corrections. J Nucl Med 2007;48: 1112–21.
[34] Cook RAH, Carnes G, Lee T-Y, et al. Respiration-averaged CT for attenuation correction in canine cardiac PET/CT. J Nucl Med 2007;48: 811–8.
[35] Osman MM, Cohade C, Nakamoto Y, et al. Clinically significant inaccurate localization of lesions with PET/CT: frequency in 300 patients. J Nucl Med 2003;44:240–3.
[36] Goerres GW, Kamel E, Seifert B, et al. Accuracy of image coregistration of pulmonary lesions in patients with nonsmall cell lung cancer using an integrated PET/CT system. J Nucl Med 2002;43:1469–75.
[37] Goerres GW, Burger C, Kamel E, et al. Respiration-induced attenuation artifact at PET/CT: technical considerations. Radiology 2003;226: 906–10.
[38] Erdi YE, Nehmeh SA, Pan T, et al. The CT motion quantitation of lung lesions and its impact on PET-measured SUVs. J Nucl Med 2004; 45:1287–92.
[39] Pan T, Mawlawi O, Nehmeh SA, et al. Attenuation correction of PET images with respiration-averaged CT images in PET/CT. J Nucl Med 2005;46:1481–7.

[40] Beyer T, Rosenbaum S, Veit P, et al. Respiration artifacts in whole-body (18)F-FDG PET/CT studies with combined PET/CT tomographs employing spiral CT technology with 1 to 16 detector rows. Eur J Nucl Med Mol Imaging 2005;32:1429–39.
[41] Pan T, Mawlawi O, Luo D, et al. Attenuation correction of PET cardiac data with low-dose average CT in PET/CT. Med Phys 2006;33: 3931–8.
[42] Chi P-CM, Mawlawi O, Nehmeh SA, et al. Design of respiration averaged CT for attenuation correction of the PET data from PET/CT. Med Phys 2007;34:2039–47.
[43] Dahlbom M, Hoffman E. Problems in signal-to-noise ratio for attenuation correction in high-resolution PET. IEEE Trans Nucl Sci 1987;34: 288–93.
[44] Jones WF, Digby WM, Luk WK, et al. Optimizing rod window width in positron emission tomography. IEEE Trans Med Imaging 1995; 14:266–70.
[45] Carson RE, Daube-Witherspoon ME, Green MV. A method for postinjection PET transmission measurements with a rotating source. J Nucl Med 1988;29:1558–67.
[46] Daube-Witherspoon M, Carson RE, Green MV. Postinjection transmission attenuation measurements for PET. IEEE Trans Nucl Sci 1988; 35:757–61.
[47] Hooper PK, Meikle SR, Eberl S, et al. Validation of postinjection transmission measurements for attenuation correction in neurological FDG-PET studies. J Nucl Med 1996;37:128–36.
[48] Thompson CJ, Ranger N, Evans AC, et al. Validation of simultaneous PET emission and transmission scans. J Nucl Med 1991;32:154–60.
[49] Meikle SR, Eberl S, Hooper PK, et al. Simultaneous emission and transmission (SET) scanning in neurological PET studies. J Comput Assist Tomogr 1997;21:487–97.
[50] Meikle SR, Bailey DL, Hooper PK, et al. Simultaneous emission and transmission measurements for attenuation correction in whole-body PET. J Nucl Med 1995;36:1680–8.
[51] Lodge MA, Badawi RD, Marsden PK. A clinical evaluation of the quantitative accuracy of simultaneous emission/transmission scanning in whole-body positron emission tomography. Eur J Nucl Med 1998;25:417–23.
[52] Watson CC, Eriksson L, Casey ME, et al. Design and performance of collimated coincidence point sources for simultaneous transmission measurements in 3-D PET. IEEE Trans Nucl Sci 2001;48:673–9.
[53] deKemp RA, Nahmias C. Attenuation correction in PET using single-photon transmission measurement. Med Phys 1994;21:771–8.
[54] Karp JS, Muehllehner G, Qu H, et al. Singles transmission in volume-imaging PET with a 137Cs source. Phys Med Biol 1995;40:929–44.
[55] Zaidi H, Diaz-Gomez M, Boudraa AE, et al. Fuzzy clustering-based segmented attenuation correction in whole-body PET imaging. Phys Med Biol 2002;47:1143–60.
[56] Watson CC, Schaefer A, Luk WK, et al. Clinical evaluation of single-photon attenuation correction for 3D whole-body PET. IEEE Trans Nucl Sci 1999;46:1024–31.
[57] de Jong HWAM, Boellaard R, Lenox M, et al. Correction for emission contamination in transmission scans for the high-resolution research tomograph. IEEE Trans Nucl Sci 2004; 51:673–6.
[58] Boudraa A, Zaidi H. Image segmentation techniques in nuclear medicine imaging. In: Zaidi H, editor. Quantitative analysis of nuclear medicine images. New York: Springer; 2006. p. 308–57.
[59] Meikle SR, Dahlbom M, Cherry SR. Attenuation correction using count-limited transmission data in positron emission tomography. J Nucl Med 1993;34:143–50.
[60] Xu M, Cutler P, Luk W. Adaptive, segmented attenuation correction for whole-body PET imaging. IEEE Trans Nucl Sci 1996;43:331–6.
[61] Bilger K, Kupferschlager J, Muller-Schauenburg W, et al. Threshold calculation for segmented attenuation correction in PET with histogram fitting. IEEE Trans Nucl Sci 2001;48:43–50.
[62] Bettinardi V, Pagani E, Gilardi M, et al. An automatic classification technique for attenuation correction in positron emission tomography. Eur J Nucl Med 1999;26:447–58.
[63] Tai Y-C, Lin K-P, Dahlbom M, et al. A hybrid attenuation correction technique to compensate for lung density in 3-D total body PET. IEEE Trans Nucl Sci 1996;43:323–30.
[64] Yu SK, Nahmias C. Segmented attenuation correction using artificial neural networks in positron tomography. Phys Med Biol 1996;41:2189–206.
[65] Reutte B, Klein GJ, Huesman RH. Automated 3-D segmentation of respiratory-gated PET transmission images. IEEE Trans Nucl Sci 1997;44:2473–6.
[66] Riddell C, Brigger P, Carson RE, et al. The watershed algorithm: a method to segment noisy PET transmission images. IEEE Trans Nucl Sci 1999; 46:713–9.
[67] Anderson JMM, Srinivasan R, Mair BA, et al. Hidden Markov model-based attenuation correction for positron emission tomography. IEEE Trans Nucl Sci 2002;49:2103–11.
[68] Fessler JA, Ficaro EP, Clinthorne NH, et al. Grouped-coordinate ascent algorithms for penalized-likelihood transmission image reconstruction. IEEE Trans Med Imaging 1997;16: 166–75.
[69] Alenius S, Ruotsalainen U, Astola J. Attenuation correction for PET using count-limited transmission images reconstructed with median root prior. IEEE Trans Nucl Sci 1999;46:646–51.

[70] Nuyts J, Dupont P, Stroobants S, et al. Simultaneous maximum a posteriori reconstruction of attenuation and activity distributions from emission sinograms. IEEE Trans Med Imaging 1999;18:393–403.
[71] Kitamura K, Iida H, Shidahara M, et al. Noise reduction in PET attenuation correction using nonlinear Gaussian filters. IEEE Trans Nucl Sci 2000;47:994–9.
[72] Pawitan Y, Bettinardi V, Teras M. Non-Gaussian smoothing of low-count transmission scans for PET whole-body studies. IEEE Trans Med Imaging 2005;24:122–9.
[73] Demirkaya O. Anisotropic diffusion filtering of PET attenuation data to improve emission images. Phys Med Biol 2002;47:N271–8.
[74] Hounsfield GN. Computerized transverse axial scanning (tomography). 1. Description of system. Br J Radiol 1973;46:1016–22.
[75] Nickoloff EL, Perman WH, Esser PD, et al. Left ventricular volume: physical basis for attenuation corrections in radionuclide determinations. Radiology 1984;152:511–5.
[76] Blankespoor SC, Xu X, Kaiki K, et al. Attenuation correction of SPECT using x-ray CT on an emission–transmission CT system: myocardial perfusion assessment. IEEE Trans Nucl Sci 1996;43:2263–74.
[77] Kinahan PE, Townsend DW, Beyer T, et al. Attenuation correction for a combined 3D PET/CT scanner. Med Phys 1998;25:2046–53.
[78] Townsend DW, Carney JPJ, Yap JT, et al. PET/CT today and tomorrow. J Nucl Med 2004;45:4S–14S.
[79] Rowell NP, Glaholm J, Flower MA, et al. Anatomically derived attenuation coefficients for use in quantitative single photon emission tomography studies of the thorax. Eur J Nucl Med 1992;19:36–40.
[80] Le Goff-Rougetet R, Frouin V, Mangin J-F, et-al. Use of segmented MR images for brain attenuation correction in PET. In: Loew MH, editor. Proc. SPIE, Newport Beach, CA, 1994. vol. 2167. p. 725–36.
[81] Zaidi H. Is MRI-guided attenuation correction a viable option for dual-modality PET/MR imaging? Radiology 2007;244:639–42.
[82] El Fakhri G, Kijewski MF, Moore SC. Absolute activity quantitation from projections using an analytical approach: comparison with iterative methods in Tc-99m and I-123 brain SPECT. IEEE Trans Nucl Sci 2001;48:768–73.
[83] Zaidi H, Montandon M-L, Slosman DO. Magnetic resonance imaging-guided attenuation and scatter corrections in three-dimensional brain positron emission tomography. Med Phys 2003;30:937–48.
[84] ICRU. Tissue substitutes in radiation dosimetry and measurement. Report No. 44. Bethesda (MD): International Commission on Radiological Units and Measurements; 1989.
[85] Dogdas B, Shattuck DW, Leahy RM. Segmentation of skull and scalp in 3-D human MRI using mathematical morphology. Hum Brain Mapp 2005;26:273–85.
[86] Burbar Z, Grazioso RF, Corbeil J, et al. PET performance of MR/PET brain insert tomograph [abstract]. In: Philips B, editor. Proc. of the IEEE Nuclear Science Symposium and Medical Imaging Conference. San Diego, October 29-November 4, 2006. San Diego, CA, 2006.
[87] Fripp J, Crozier S, Warfield SK, et al. Automatic segmentation of the bone and extraction of the bone & cartilage interface from magnetic resonance images of the knee. Phys Med Biol 2007;52:1617–31.
[88] Martinez-Moller A, Souvatzoglou M, Botnar R, et al. An approach for MR-based attenuation correction for combined MR/PET: effects of ignoring bones [abstract]. J Nucl Med 2007;48:156.
[89] Steinberg J, Zhang J, Sammet S, et al. Attenuation maps for PET reconstruction using MRI-based segmentation [abstract]. J Nucl Med 2007;48:412P.
[90] Robson MD, Gatehouse PD, Bydder M, et al. Magnetic resonance: an introduction to ultrashort TE (UTE) imaging. J Comput Assist Tomogr 2003;27:825–46.
[91] Robson MD, Bydder GM. Clinical ultrashort echo time imaging of bone and other connective tissues. NMR Biomed 2006;19:765–80.
[92] Kadrmas DJ, Rust TC. Feasibility of rapid multitracer PET tumor imaging. IEEE Trans Nucl Sci 2005;52:1341–7.
[93] Rust TC, Kadrmas DJ. Rapid dual-tracer PTSM+ATSM PET imaging of tumour blood flow and hypoxia: a simulation study. Phys Med Biol 2006;51:61–75.
[94] Ray N, Acton ST, Altes T, et al. Merging parametric active contours within homogeneous image regions for MRI-based lung segmentation. IEEE Trans Med Imaging 2003;22:189–99.
[95] Heverhagen JT, Hahn HK, Wegmann M, et al. Volumetric analysis of mice lungs in a clinical magnetic resonance imaging scanner. MAGMA 2004;17:80–5.
[96] Plathow C, Schoebinger M, Fink C, et al. Evaluation of lung volumetry using dynamic three-dimensional magnetic resonance imaging. Invest Radiol 2005;40:173–9.
[97] Böttger T, Grunewald K, Schöbinger M, et al. Implementation and evaluation of a new workflow for registration and segmentation of pulmonary MRI data for regional lung perfusion assessment. Phys Med Biol 2007;52:1261–75.
[98] Sensakovic WF, Armato SG III, Starkey A, et al. Automated lung segmentation of diseased and artifact-corrupted magnetic resonance sections. Med Phys 2006;33:3085–93.
[99] Lelieveldt BP, van der Geest RJ, Rezaee MR, et al. Anatomical model matching with fuzzy implicit surfaces for segmentation of thoracic volume scans. IEEE Trans Med Imaging 1999;18:218–30.
[100] Robinson PJ, Kreel L. Pulmonary tissue attenuation with computed tomography: comparison

of inspiration and expiration scans. J Comput Assist Tomogr 1979;3:740–8.
[101] Montandon M-L, Zaidi H. Atlas-guided nonuniform attenuation correction in cerebral 3D PET imaging. Neuroimage 2005;25:278–86.
[102] Hofmann M, Steinke F, Scheel V, et al. MR-based PET attenuation correction—method and validation. Proc. IEEE Nuclear Science Symposium and Medical Imaging Conference, 30 Oct. - 03 Nov. 2007; Honolulu, Hawaii, USA.
[103] Bronnikov AV. Reconstruction of attenuation map using discrete consistency conditions. IEEE Trans Med Imaging 2000;19:451–62.
[104] Panin VY, Kehren F, Hamill J, et al. Application of discrete data consistency conditions for selecting regularization parameters in PET attenuation map reconstruction. Phys Med Biol 2004;49:2425–36.
[105] Kamel E, Hany TF, Burger C, et al. CT vs 68Ge attenuation correction in a combined PET/CT system: evaluation of the effect of lowering the CT tube current. Eur J Nucl Med Mol Imaging 2002;29:346–50.
[106] Chin BB, Patel PV, Nakamoto Y, et al. Quantitative evaluation of 2-deoxy-2-[18F] fluoro-D-glucose uptake in hepatic metastases with combined PET-CT: iterative reconstruction with CT attenuation correction versus filtered back projection with 68Germanium attenuation correction. Mol Imaging Biol 2002;4:399–409.
[107] Goerres GW, Schmid DT, Eyrich GK. Do hardware artifacts influence the performance of head and neck PET scans in patients with oral cavity squamous cell cancer? Dentomaxillofac Radiol 2003;32:365–71.
[108] Nakamoto Y, Osman M, Cohade C, et al. PET/CT: comparison of quantitative tracer uptake between germanium and CT transmission attenuation-corrected images. J Nucl Med 2002;43:1137–43.
[109] Burger C, Goerres G, Schoenes S, et al. PET attenuation coefficients from CT images: experimental evaluation of the transformation of CT into PET 511-keV attenuation coefficients. Eur J Nucl Med Mol Imaging 2002;29:922–7.
[110] Visvikis D, Costa DC, Croasdale I, et al. CT-based attenuation correction in the calculation of semiquantitative indices of [^{18}F]-FDG uptake in PET. Eur J Nucl Med 2003;30:344–53.
[111] Koepfli P, Hany TF, Wyss CA, et al. CT attenuation correction for myocardial perfusion quantification using a PET/CT hybrid scanner. J Nucl Med 2004;45:537–42.
[112] Fitzpatrick GM, Wells RG. Simulation study of respiratory-induced errors in cardiac positron emission tomography/computed tomography. Med Phys 2006;33:2888–95.
[113] Souvatzoglou M, Ziegler SI, Martinez MJ, et al. Standardised uptake values from PET/CT images: comparison with conventional attenuation-corrected PET. Eur J Nucl Med Mol Imaging 2007;34:405–12.
[114] van Dalen JA, Visser EP, Vogel WV, et al. Impact of Ge-68/Ga-68-based versus CT-based attenuation correction on PET. Med Phys 2007;34:889–97.
[115] Papathanassiou D, Becker S, Amir R, et al. Respiratory motion artifact in the liver dome on FDG PET/CT: comparison of attenuation correction with CT and a caesium external source. Eur J Nucl Med Mol Imaging 2005;32:1422–8.
[116] Mirzaei S, Guerchaft M, Bonnier C, et al. Use of segmented CT transmission map to avoid metal artifacts in PET images by a PET-CT device. BMC Nucl Med 2005;5:3.
[117] Novikov RG. An inversion formula for the attenuated x-ray transformation. Ark Mat 2002;40:145–67.
[118] Novikov RG. On the range characterization for the two-dimensional attenuated x-ray transformation. Inverse Probl 2002;18:677–700.
[119] Natterer F. Inversion of the attenuated radon transform. Inverse Problems 2001;17:113–9.
[120] Boman J, Stromberg J-O. Novikov's inversion formula for the attenuated radon transform—a new approach. J Geom Anal 2004;14:185–98.
[121] Michel C, Sibomana M, Boi A, et al. Preserving Poisson characteristics of PET data with weighted OSEM reconstruction. Conf. Rec. of IEEE Nuclear Science Symposium and Medical Imaging Conference, Toronto, ON, 8-14 November, 1998;2:1323–9.
[122] Lartizien C, Kinahan PE, Swensson R, et al. Evaluating image reconstruction methods for tumor detection in 3-dimensional whole-body PET oncology imaging. J Nucl Med 2003;44:276–90.
[123] Levin C, Zaidi H. Current trends in preclinical PET system design. PET Clinics, in press.
[124] Chow PL, Rannou FR, Chatziioannou AF. Attenuation correction for small animal PET tomographs. Phys Med Biol 2005;50:1837–50.
[125] Tai YC, Ruangma A, Rowland D, et al. Performance evaluation of the micro-PET focus: a third-generation micro-PET scanner dedicated to animal imaging. J Nucl Med 2005;46:455–63.
[126] Fahey FH, Gage HD, Buchheimer N, et al. Evaluation of the quantitative capability of a high-resolution positron emission tomography scanner for small animal imaging. J Comput Assist Tomogr 2004;28:842–8.
[127] Lehnert W, Meikle SR, Siegel S, et al. Evaluation of transmission methodology and attenuation correction for the micro-PET Focus 220 animal scanner. Phys Med Biol 2006;51:4003–16.
[128] Vandervoort E, Camborde M-L, Jan S, et al. Monte Carlo modeling of singles-mode transmission data for small animal PET scanners. Phys Med Biol 2007;52:3169–84.
[129] Thompson CJ, Lecomte R, Cadorette J. Feasibility of using beta-gamma coincidence for 3D PET attenuation correction. IEEE Trans Nucl Sci 2000;47:1176–81.

[130] Camborde M-L, Thompson CJ, Togane D, et al. A positron decay-triggered transmission source for positron emission tomography. IEEE Trans Nucl Sci 2004;51:53–7.
[131] Ritman EL. Molecular imaging in small animals—roles for micro-CT. J Cell Biochem Suppl 2002;39:116–24.
[132] Hwang A, Hasegawa B. Attenuation correction for small animal SPECT imaging using x-ray CT data. Med Phys 2005;32:2799–804.
[133] Hwang AB, Taylor CC, Vanbrocklin HF, et al. Attenuation correction of small animal SPECT images acquired with 125I-Iodorotenone. IEEE Trans Nucl Sci 2006;53:1213–20.
[134] Chow PL, Stout DB, Komisopoulou E, et al. A method of image registration for small animal, multimodality imaging. Phys Med Biol 2006;51:379–90.
[135] Goertzen AL, Meadors AK, Silverman RW, et al. Simultaneous molecular and anatomical imaging of the mouse in vivo. Phys Med Biol 2002; 21:4315–28.
[136] Fontaine R, Belanger F, Cadorette J, et al. Architecture of a dual-modality, high-resolution, fully digital positron emission tomography/computed tomography (PET/CT) scanner for small animal imaging. IEEE Trans Nucl Sci 2005;52:691–6.
[137] Liang H, Yang Y, Yang K, et al. A micro-PET/CT system for in vivo small animal imaging. Phys Med Biol 2007;52:3881–94.
[138] Yao R, Seidel J, Liow J-S, et al. Attenuation correction for the NIH ATLAS small animal PET scanner. IEEE Trans Nucl Sci 2005;52: 664–8.
[139] Beyer T, Antoch G, Bockisch A, et al. Optimized intravenous contrast administration for diagnostic whole-body 18F-FDG PET/CT. J Nucl Med 2005;46:429–35.
[140] Brechtel K, Klein M, Vogel M, et al. Optimized contrast-enhanced CT protocols for diagnostic whole-body 18F-FDG PET/CT: technical aspects of single-phase versus multiphase CT imaging. J Nucl Med 2006;47:470–6.
[141] Nagel CCA, Bosmans G, Dekker ALAJ, et al. Phased attenuation correction in respiration correlated computed tomography/positron emitted tomography. Med Phys 2006;33: 1840–7.
[142] Li T, Thorndyke B, Schreibmann E, et al. Model-based image reconstruction for four-dimensional PET. Med Phys 2006;33:1288–98.
[143] Lamare F, Cresson T, Savean J, et al. Respiratory motion correction for PET oncology applications using affine transformation of list mode data. Phys Med Biol 2007;52:121–40.
[144] Lewitt RM, Bates RHT. Image reconstruction from projections: III projection completion methods (theory). Optik 1978;50:189–204.
[145] Kalender WA, Hebel R, Ebersberger J. Reduction of CT artifacts caused by metallic implants. Radiology 1987;164:576–7.
[146] Tuy HK. A postprocessing algorithm to reduce metallic clip artifacts in CT images. Eur Radiol 1993;V3:129–34.
[147] Glover GH, Pelc NJ. An algorithm for the reduction of metal clip artifacts in CT reconstructions. Med Phys 1981;8:799–807.
[148] Klotz E, Kalender WA, Sokiransky R, et al. Algorithms for the reduction of CT artifacts caused by metallic implants. In: Dwyer SJ, Jost RG, editors. Medical imaging IV: PACS systems design and evaluation 1990;1234:642–50.
[149] Wang G, Snyder DL, O'Sullivan JA, et al. Iterative deblurring for CT metal artifact reduction. IEEE Trans Med Imaging 1996;15:657–64.
[150] Williamson JF, Whiting BR, Benac J, et al. Prospects for quantitative computed tomography imaging in the presence of foreign metal bodies using statistical image reconstruction. Med Phys 2002;29:2404–18.
[151] Soltanian-Zadeh H, Windham JP, Soltanian-Zadeh J. CT artifact correction: an image-processing approach. In: Loew MH, Hanson KM, editors. Medical Imaging 1996:2710:477–85.
[152] Wei J, Chen L, Sandison GA, et al. X-ray CT high-density artifact suppression in the presence of bones. Phys Med Biol 2004;49: 5407–18.
[153] Mahnken AH, Raupach R, Wildberger JE, et al. A new algorithm for metal artifact reduction in computed tomography: in vitro and in vivo evaluation after total hip replacement. Invest Radiol 2003;38:769–75.
[154] Robertson DD, Yuan J, Wang G, et al. Total hip prosthesis metal artifact suppression using iterative deblurring reconstruction. J Comput Assist Tomogr 1997;21:293–8.
[155] Wang G, Frei T, Vannier MW. Fast iterative algorithm for metal artifact reduction in x-ray CT. Acad Radiol 2000;7:607–14.
[156] Zhao S, Robertson DD, Wang G, et al. X-ray CT metal artifact reduction using wavelets: an application for imaging total hip prostheses. IEEE Trans Med Imaging 2000;19:1238–47.
[157] De Man B, Nuyts J, Dupont P, et al. Metal streak artifacts in x-ray computed tomography: a simulation study. IEEE Trans Nucl Sci 1999;46:691–6.
[158] De Man B, Nuyts J, Dupont P, et al. Reduction of metal streak artifacts in x-ray computed tomography using a transmission maximum a posteriori algorithm. IEEE Trans Nucl Sci 2000;47:977–81.
[159] De Man B, Nuyts J, Dupont P, et al. An iterative maximum-likelihood polychromatic algorithm for CT. IEEE Trans Med Imaging 2001;20: 999–1008.
[160] Hamill JJ, Brunken RC, Bybel B, et al. A knowledge-based method for reducing attenuation artifacts caused by cardiac appliances in myocardial PET/CT. Phys Med Biol 2006;51: 2901–18.
[161] Lemmens C, Faul D, Hamill J, et al. Suppression of metal streak artifacts in CT using

a MAP reconstruction procedure. IEEE Nuclear Science Symposium Conference Record 2006; 6:3431–7.
[162] Bal M, Spies L. Metal artifact reduction in CT using tissue class modeling and adaptive prefiltering. Med Phys 2006;33:2852–9.
[163] Kalvin AD. System and method for reducing reconstruction artifacts in computed tomography images. United States Patent 5933471, 1999. Available at: http://www.freepatentsonline.com/5933471.html.
[164] Watzke O, Kalender WA. A pragmatic approach to metal artifact reduction in CT: merging of metal artifact reduced images. Eur Radiol 2004;14:849–56.
[165] Lemmens C, Montandon M-L, Nuyts J, et al. Impact of metal artifacts due to EEG electrodes in brain PET imaging. Proc. IEEE Nuclear Science Symposium and Medical Imaging Conference, 30 Oct. - 03 Nov. 2007; Honolulu, Hawaii, USA, in press.
[166] Michel C, Noo F, Sibomana M, et al. An iterative method for creating attenuation maps from highly truncated CT data. Conf. Proc. of the VIIth International Meeting on Fully Three-dimensional Image Reconstruction in Radiology and Nuclear Medicine, Utah, USA, 2005:88–91.
[167] Beyer T, Bockisch A, Kuhl H, et al. Whole-body 18F-FDG PET/CT in the presence of truncation artifacts. J Nucl Med 2006;47:91–9.
[168] Mawlawi O, Erasmus JJ, Pan T, et al. Truncation artifact on PET/CT: impact on measurements of activity concentration and assessment of a correction algorithm. AJR Am J Roentgenol 2006; 186:1458–67.
[169] Sourbelle K, Kachelriess M, Kalender WA. Reconstruction from truncated projections in CT using adaptive detruncation. Eur Radiol 2005;15:1008–14.
[170] Zamyatin AA, Nakanishi S. Extension of the reconstruction field of view and truncation correction using sinogram decomposition. Med Phys 2007;34:1593–604.
[171] Hsieh J, Molthen RC, Dawson CA, et al. An iterative approach to the beam hardening correction in cone beam CT. Med Phys 2000;27:23–9.
[172] Kachelriess M, Sourbelle K, Kalender WA. Empirical cupping correction: a first-order raw data precorrection for cone beam computed tomography. Med Phys 2006;33:1269–74.
[173] Malusek A, Seger MM, Sandborg M, et al. Effect of scatter on reconstructed image quality in cone beam computed tomography: evaluation of a scatter reduction optimisation function. Radiat Prot Dosimetry 2005;114:337–40.
[174] Siewerdsen JH, Daly MJ, Bakhtiar B, et al. A simple, direct method for x-ray scatter estimation and correction in digital radiography and cone beam CT. Med Phys 2006;33:187–97.
[175] Zbijewski W, Beekman FJ. Efficient Monte Carlo based scatter artifact reduction in cone beam micro-CT. IEEE Trans Med Imaging 2006;25:817–27.
[176] Ay M, Zaidi H. Assessment of errors caused by x-ray scatter and use of contrast medium when using CT-based attenuation correction in PET. Eur J Nucl Med Mol Imaging 2006;33:1301–13.
[177] Beyer T, Kinahan PE, Townsend DW, et al. The use of X-ray CT for attenuation correction of PET data. Proc. IEEE Nuclear Science Symposium and Medical Imaging Conference, 30 Oct.-5 Nov., Norfolk, VA, USA, 4:1573–7.
[178] Bai C, Shao L, Da Silva AJ, et al. A generalized model for the conversion from CT numbers to linear attenuation coefficients. IEEE Trans Nucl Sci 2003;50:1510–5.
[179] Guy MJ, Castellano-Smith IA, Flower MA, et al. DETECT dual-energy transmission estimation CT for improved attenuation correction in SPECT and PET. IEEE Trans Nucl Sci 1998;45:1261–7.
[180] Kinahan PE, Alessio AM, Fessler JA. Dual-energy CT attenuation correction methods for quantitative assessment of response to cancer therapy with PET/CT imaging. Technol Cancer Res Treat 2006;5:319–27.
[181] Flohr TG, McCollough CH, Bruder H, et al. First performance evaluation of a dual-source CT (DSCT) system. Eur Radiol 2006;16:256–68.
[182] Greess H, Lutze J, Nomayr A, et al. Dose reduction in subsecond multislice spiral CT examination of children by online tube current modulation. Eur Radiol 2004;14:995–9.
[183] Wang J, Li T, Lu H, et al. Noise reduction for low-dose single-slice helical CT sinograms. IEEE Trans Nucl Sci 2006;53:1230–7.
[184] Ay M, Zaidi H. Impact of x-ray tube settings and metallic leads on neurological PET imaging when using CT-based attenuation correction. Nucl Instrum Methods Phys Res A 2007;571: 411–4.
[185] Ay M, Zaidi H. Computed tomography-based attenuation correction in neurological positron emission tomography: evaluation of the effect of x-ray tube voltage on quantitative analysis. Nucl Med Commun 2006;27:339–46.
[186] Carney JP, Townsend DW, Rappoport V, et al. Method for transforming CT images for attenuation correction in PET/CT imaging. Med Phys 2006;33:976–83.
[187] Shikhaliev PM. Beam hardening artifacts in computed tomography with photon counting, charge integrating and energy weighting detectors: a simulation study. Phys Med Biol 2005; 50:5813–27.
[188] Alles J, Mudde RF. Beam hardening: analytical considerations of the effective attenuation coefficient of x-ray tomography. Med Phys 2007;34: 2882–9.
[189] Kanamori H, Nakamori N, Inoue K, et al. Effect of scattered x-ray on CT images. Phys Med Biol 1985;30:239–49.
[190] Kachelriess M, Kalender WA. Improving PET/CT attenuation correction with iterative CT beam

hardening correction. IEEE Nuclear Science Symposium Conference Record San Juan, Puerto Rico, October 23–29, 2005;4:5.
[191] Krishnasetty V, Fischman AJ, Halpern EL, et al. Comparison of alignment of computer-registered data sets: combined PET/CT versus independent PET and CT of the thorax. Radiology 2005;237: 635–9.
[192] Xing L, Wessels B. The value of PET/CT is being oversold as a clinical tool in radiation oncology. Med Phys 2005;32:1457–9.
[193] Beyer T, Townsend D. Putting clear into nuclear medicine: a decade of PET/CT development [editorial]. Eur J Nucl Med Mol Imaging 2006;33:857–61.
[194] Zaidi H. The quest for the ideal anato–molecular imaging fusion tool. Biomed Imaging Interv J 2006;2:e47.
[195] Alavi A, Mavi A, Basu S, et al. Is PET-CT the only option? Eur J Nucl Med Mol Imaging 2007;34: 819–21.
[196] Rahmim A, Rousset OG, Zaidi H. Strategies for motion tracking and correction in PET. PET Clinics, in press.
[197] Pietrzyk U. Does PET/CT render software fusion obsolete? Nuklearmedizin 2005;44:S13–7.
[198] Visvikis D, Lamare F, Bruyant P, et al. Respiratory motion in positron emission tomography for oncology applications: problems and solutions. Nucl Instr Meth A 2006;569: 453–7.
[199] Cohade C, Osman M, Marshall LN, et al. PET-CT: accuracy of PET and CT spatial registration of lung lesions. Eur J Nucl Med Mol Imaging 2003;30:721–6.
[200] Nakamoto Y, Chin BB, Cohade C, et al. PET/CT: artifacts caused by bowel motion. Nucl Med Commun 2004;25:221–5.
[201] Cohade C, Wahl RL. Applications of positron emission tomography/computed tomography image fusion in clinical positron emission tomography - clinical use, interpretation, methods, diagnostic improvements. Semin Nucl Med 2003;33: 228–37.
[202] Osman MM, Cohade C, Nakamoto Y, et al. Respiratory motion artifacts on PET emission images obtained using CT attenuation correction on PET-CT. Eur J Nucl Med Mol Imaging 2003;30:603–6.
[203] Goerres GW, Kamel E, Heidelberg TN, et al. PET-CT image coregistration in the thorax: influence of respiration. Eur J Nucl Med Mol Imaging 2002;29:351–60.
[204] Pevsner A, Nehmeh SA, Humm JL, et al. Effect of motion on tracer activity determination in CT attenuation corrected PET images: a lung phantom study. Med Phys 2005;32: 2358–62.
[205] Nehmeh SA, Erdi YE, Ling CC, et al. Effect of respiratory gating on reducing lung motion artifacts in PET imaging of lung cancer. Med Phys 2002;29:366–71.
[206] Nehmeh SA, Erdi YE, Ling CC, et al. Effect of respiratory gating on quantifying PET images of lung cancer. J Nucl Med 2002;43:876–81.
[207] Nehmeh SA, Erdi YE, Pan T, et al. Four-dimensional (4D) PET/CT imaging of the thorax. Med Phys 2004;31:3179–86.
[208] Nehmeh SA, Erdi YE, Pan T, et al. Quantitation of respiratory motion during 4D-PET/CT acquisition. Med Phys 2004;31:1333–8.
[209] Nehmeh SA, Erdi YE, Meirelles GS, et al. Deep inspiration breath-hold PET/CT of the thorax. J Nucl Med 2007;48:22–6.
[210] Sarikaya I, Yeung HW, Erdi Y, et al. Respiratory artifact causing malpositioning of liver dome lesion in right lower lung. Clin Nucl Med 2003;28:943–4.
[211] Conti M, Bendriem B, Casey M. Performance of a high sensitivity PET scanner-based on LSO panel detectors. IEEE Trans Nucl Sci 2006;53: 1136–42.
[212] Fitton I, Steenbakkers RJHM, Zijp L, et al. Retrospective attenuation correction of PET data for radiotherapy planning using a free-breathing CT. Radiother Oncol 2007;83:42–8.
[213] Gilman MD, Fischman AJ, Krishnasetty V, et al. Optimal CT breathing protocol for combined thoracic PET/CT. AJR Am J Roentgenol 2006; 187:1357–60.
[214] Nye JA, Esteves F, Votaw JR. Minimizing artifacts resulting from respiratory and cardiac motion by optimization of the transmission scan in cardiac PET/CT. Med Phys 2007;34:1901–6.
[215] Alessio AM, Kohlmyer S, Branch K, et al. Cine CT for attenuation correction in cardiac PET/CT. J Nucl Med 2007;48:794–801.
[216] Nehmeh SA, Erdi YE, Rosenzweig KE, et al. Reduction of respiratory motion artifacts in PET imaging of lung cancer by respiratory correlated dynamic PET: methodology and comparison with respiratory gated PET. J Nucl Med 2003;44:1644–8.
[217] Mageras GS, Pevsner A, Yorke ED, et al. Measurement of lung tumor motion using respiration-correlated CT. Int J Radiat Oncol Biol Phys 2004;60:933–41.
[218] Meirelles GSP, Erdi YE, Nehmeh SA, et al. Deep inspiration breath-hold PET/CT: clinical findings with a new technique for detection and characterization of thoracic lesions. J Nucl Med 2007;48:712–9.
[219] Boucher L, Rodrigue S, Lecomte R, et al. Respiratory gating for 3-dimensional PET of the thorax: feasibility and initial results. J Nucl Med 2004;45:214–9.
[220] Martinez-Möller A, Zikic D, Botnar R, et al. Dual cardiac respiratory gated PET: implementation and results from a feasibility study. Eur J Nuc Med Mol Imaging 2007;34:1447–54.
[221] Klein GJ, Reutter BW, Ho MH, et al. Real-time system for respiratory–cardiac gating in positron tomography. IEEE Trans Nucl Sci 1998;45: 2139–43.

[222] Le Meunier L, Maass-Moreno R, Carrasquillo JA, et al. PET/CT imaging: effect of respiratory motion on apparent myocardial uptake. J Nucl Cardiol 2006;13:821–30.
[223] Martinez-Moller A, Souvatzoglou M, Navab N, et al. Artifacts from misaligned CT in cardiac perfusion PET/CT studies: frequency, effects, and potential solutions. J Nucl Med 2007;48: 188–93.
[224] Takahashi Y, Murase K, Higashino H, et al. Attenuation correction of myocardial SPECT images with x-ray CT: effects of registration errors between x-ray CT and SPECT. Ann Nucl Med 2002;16:431–5.
[225] Goetze S, Pannu HK, Wahl RL. Clinically significant abnormal findings on the nondiagnostic CT portion of low-amperage CT attenuation-corrected myocardial perfusion SPECT/CT studies. J Nucl Med 2006;47:1312–8.
[226] Goetze S, Brown TL, Lavely WC, et al. Attenuation correction in myocardial perfusion SPECT/CT: effects of misregistration and value of reregistration. J Nucl Med 2007;48:1090–5.
[227] Graf S, Khorsand A, Stix G, et al. Attenuation correction for myocardial perfusion imaging. A comparison between SPECT and PET imaging by polar map analysis. Nuklearmedizin 2006; 45:171–6.
[228] Antoch G, Freudenberg LS, Beyer T, et al. To enhance or not to enhance? 18F-FDG and CT contrast agents in dual-modality 18F-FDG PET/CT. J Nucl Med 2004;(45 Suppl 1):56S–65S.
[229] Schaefer NG, Hany TF, Taverna C, et al. Non-Hodgkin lymphoma and Hodgkin disease: coregistered FDG PET and CT at staging and restaging—do we need contrast-enhanced CT? Radiology 2004;232:823–9.
[230] Strobel K, Thuerl C, Hany T. How much intravenous contrast is needed in FDG-PET/CT? Nuklearmedizin 2005;44:S32–7.
[231] Yau Y-Y, Chan W-S, Tam Y-M, et al. Application of intravenous contrast in PET/CT: does it really introduce significant attenuation correction error? J Nucl Med 2005;46:283–91.
[232] Berthelsen AK, Holm S, Loft A, et al. PET/CT with intravenous contrast can be used for PET attenuation correction in cancer patients. Eur J Nucl Med Mol Imaging 2005;32:1167–75.
[233] Groves AM, Kayani I, Dickson JC, et al. Oral contrast medium in PET/CT: should you or shouldn't you? Eur J Nucl Med Mol Imaging 2005;32:1160–6.
[234] von Schulthess GK, Veit-Haibach P. Quid des produits de contraste en TEP/TDM? Medecine Nucleaire 2007;31:202–5.
[235] Gollub MJ, Hong R, Sarasohn DM, et al. Limitations of CT during PET/CT. J Nucl Med 2007; 48:1583–91.
[236] Pfannenberg AC, Aschoff P, Brechtel K, et al. Low-dose nonenhanced CT versus standard dose contrast-enhanced CT in combined PET/CT protocols for staging and therapy planning in nonsmall cell lung cancer. Eur J Nuc Med Mol Imaging 2007;V34:36–44.
[237] Tateishi U, Maeda T, Morimoto T, et al. Nonenhanced CT versus contrast-enhanced CT in integrated PET/CT studies for nodal staging of rectal cancer. Eur J Nuc Med Mol Imaging 2007;34:1627–34.
[238] Rodriguez-Vigil B, Gomez-Leon N, Pinilla I, et al. PET/CT in lymphoma: prospective study of enhanced full-dose PET/CT versus unenhanced low-dose PET/CT. J Nucl Med 2006; 47:1643–8.
[239] Rodriguez-Vigil B, Gomez-Leon N, Pinilla I, et al. Positron emission tomography/computed tomography in the management of Hodgkin's disease and non-Hodgkin's lymphoma. Curr Probl Diagn Radiol 2006;35:151–63.
[240] Antoch G, Kuehl H, Kanja J, et al. Dual-modality PET/CT scanning with negative oral contrast agent to avoid artifacts: introduction and evaluation. Radiology 2004;230:879–85.
[241] Dizendorf E, Hany TF, Buck A, et al. Cause and magnitude of the error induced by oral CT contrast agent in CT-based attenuation correction of PET emission studies. J Nucl Med 2003; 44:732–8.
[242] Nehmeh SA, Erdi YE, Kalaigian H, et al. Correction for oral contrast artifacts in CT attenuation-corrected PET images obtained by combined PET/CT. J Nucl Med 2003;44:1940–4.
[243] Nakamoto Y, Chin BB, Kraitchman DL, et al. Effects of nonionic intravenous contrast agents at PET/CT imaging: phantom and canine studies. Radiology 2003;227:817–24.
[244] Carney J, Beyer T, Brasse D, et al. CT-based attenuation correction for PET/CT scanners in the presence of contrast agent. IEEE Nuclear Science Symposium Conference Record 2002; 3:1443–6.
[245] Otsuka H, Graham MM, Kubo A, et al. The effect of oral contrast on large bowel activity in FDG-PET/CT. Ann Nucl Med 2005;19: 101–8.
[246] Bidgoli J, Ay M, Sarkar S, et al. Correction of oral contrast artifacts in CT-based attenuation correction of PET images using an automated segmentation algorithm. IEEE Nuclear Science Symposium Conference Record, 30 Oct. - 03 Nov. 2007; Honolulu, Hawaii, USA, in press.
[247] Tang HR, Brown JK, Da Silva AJ, et al. Implementation of a combined x-ray CT-scintillation camera imaging system for localizing and measuring radionuclide uptake: experiments in phantoms and patients. IEEE Trans Nucl Sci 1999;46:551–7.
[248] Lonn AHR. Evaluation of method to minimize the effect of x-ray contrast in PET-CT attenuation correction. Nuclear Science Symposium Conference Record, 2003 IEEE, Portland, USA, 2003;3:2220–1.
[249] Buther F, Stegger L, Dawood M, et al. Effective methods to correct contrast agent-induced

errors in PET quantification in cardiac PET/CT. J Nucl Med 2007;48:1060–8.
[250] Goerres GW, Hany TF, Kamel E, et al. Head and neck imaging with PET and PET/CT: artifacts from dental metallic implants. Eur J Nucl Med Mol Imaging 2002;29:367–70.
[251] Kamel EM, Burger C, Buck A, et al. Impact of metallic dental implants on CT-based attenuation correction in a combined PET/CT scanner. Eur Radiol 2003;13:724–8.
[252] Heiba SI, Luo J, Sadek S, et al. Attenuation-correction induced artifact in F-18 FDG PET imaging following total knee replacement. Clin Positron Imaging 2000;3:237–9.
[253] Goerres GW, Ziegler SI, Burger C, et al. Artifacts at PET and PET/CT caused by metallic hip prosthetic material. Radiology 2003;226:577–84.
[254] Halpern BS, Dahlbom M, Waldherr C, et al. Cardiac pacemakers and central venous lines can induce focal artifacts on CT-corrected PET images. J Nucl Med 2004;45:290–3.
[255] DiFilippo FP, Brunken RC. Do implanted pacemaker leads and ICD leads cause metal-related artifact in cardiac PET/CT? J Nucl Med 2005;46: 436–43.
[256] Coolens C, Childs PJ. Calibration of CT Hounsfield units for radiotherapy treatment planning of patients with metallic hip prostheses: the use of the extended CT-scale. Phys Med Biol 2003; 48:1591–603.
[257] Robertson DD, Weiss PJ, Fishman EK, et al. Evaluation of CT techniques for reducing artifacts in the presence of metallic orthopedic implants. J Comput Assist Tomogr 1988;12: 236–41.
[258] Yu H, Zeng K, Bharkhada DK, et al. A segmentation-based method for metal artifact reduction. Acad Radiol 2007;14:495–504.
[259] Olive C, Klaus M, Pekar V, et al. Segmentation aided adaptive filtering for metal artifact reduction in radio-therapeutic CT images. Proc Soc Photo Opt Instrum Eng 2004;5370:1991–2002.
[260] Reader A, Zaidi H. Advances in PET image reconstruction. PET Clinics, in press.
[261] Thompson CJ, Dagher A, Lunney DN, et al. A technique to reject scattered radiation in PET transmission scans. International workshop on physics and engineering of computerized multidimensional imaging and processing. Proc Soc Photo Opt Instrum Eng 1986;671:244–53.
[262] Wegmann K, Adam L-E, Livieratos L, et al. Investigation of the scatter contribution in single photon transmission measurements by means of Monte Carlo simulations. IEEE Trans Nucl Sci 1999;46:1184–90.
[263] Joseph PM, Spital RD. The effects of scatter in x-ray computed tomography. Med Phys 1982; 9:464–72.
[264] Merritt RB, Chenery SG. Quantitative CT measurements: the effect of scatter acceptance and filter characteristics on the EMI 7070. Phys Med Biol 1986;31:55–63.
[265] Ohnesorge B, Flohr T, Klingenbeck-Regn K. Efficient object scatter correction algorithm for third- and fourth-generation CT scanners. Eur Radiol 1999;9:563–9.
[266] Endo M, Tsunoo T, Nakamori N, et al. Effect of scatter radiation on image noise in cone beam CT. Med Phys 2001;28:469–74.
[267] Rinkel J, Gerfault L, Estève F, et al. A new method for x-ray scatter correction: first assessment on a cone-beam CT experimental setup. Phys Med Biol 2007;52:4633–52.
[268] Endo M, Mori S, Tsunoo T, et al. Magnitude and effects of x-ray scatter in a 256-slice CT scanner. Med Phys 2006;33:3359–68.
[269] Wiegert J, Bertram M, Rose G, et al. Model-based scatter correction for cone beam computed tomography. Proc Soc Photo Opt Instrum Eng 2005;5745:271–82.
[270] Siewerdsen JH, Jaffray DA. Cone beam computed tomography with flat-panel imager: magnitude and effects of x-ray scatter. Med Phys 2001;28:220–31.
[271] Ning R, Tang X. X-ray scatter correction algorithm for cone beam CT imaging. Med Phys 2004;31:1195–202.
[272] Kyriakou Y, Kalender WA. X-ray scatter data for flat-panel detector CT. Phys Med 2007;23:3–15.
[273] Zhu L, Bennett NR, Fahrig R. Scatter correction method for x-ray CT using primary modulation: theory and preliminary results. IEEE Trans Med Imaging 2006;25:1573–87.
[274] Bertram M, Wiegert J, Rose G. Potential of software-based scatter corrections in cone beam volume CT. Proc Soc Photo Opt Instrum Eng 2005;5745:259–70.